CCFE
CULHAM CENTRE FOR FUSION ENERGY

UK Atomic Energy Authority

UKAEA-CCFE-PR(25)328

A. Leide, A. Martinez-Pechero, G. Clark, C. Bearcroft, O. Gavalda-Diaz, S. Robertson, E. Demir, Y. Zayachuk, A. Widdowson, E. Tarleton, J. Wade-Zhu

Progress towards a micro fibre push-out method for measuring fibre-matrix interface properties in SiC composites

Progress towards a micro fibre push-out method for measuring fibre-matrix interface properties in SiC composites

A. Leide, A. Martinez-Pechero, G. Clark, C. Bearcroft, O. Gavalda-Diaz, S. Robertson, E. Demir, Y. Zayachuk, A. Widdowson, E. Tarleton, J. Wade-Zhu

This is a preprint of a paper submitted for publication in Journal of the European Ceramic Society

Progress towards a micro fibre push-out method for measuring fibre-matrix interface properties in SiC composites

Alex Leide[a,*], Alvaro Martinez-Pechero[a,b], George Clark[a], Christopher Bearcroft[a,c], Oriol Gavalda-Diaz[d], Stuart Robertson[e], Eralp Demir[b], Yevhen Zayachuk[a], Anna Widdowson[a], Edmund Tarleton[b], James Wade-Zhu[a]

[a]*UK Atomic Energy Authority, Culham Campus, Abingdon, Oxfordshire, UK.*
[b]*Department of Engineering Science, University of Oxford, Parks Road, Oxford, UK.*
[c]*Idaho National Laboratory, Idaho Falls, ID, USA.*
[d]*Department of Materials, Royal School of Mines, Imperial College London, London, UK.*
[e]*Loughborough Materials Characterisation Centre, Loughborough University, Loughborough Leicestershire, UK.*

Abstract

Experiments and finite element modelling have been used to explore a method for miniaturising fibre push-out testing to the scale of thin ion irradiated layers. Correlation of interfacial surface area to debond stress has been identified for short fibres, and is related to a size effect following a Weibull distribution. Weibull analysis may be used to provide size-independent interfacial properties for use in engineering scale models. Various parameters have been assessed for their relative importance: axial misorientation of fibres appears to have a negligible effect on push-out characteristics while the taper of fibres does not alter the debond stress, but does alter the frictional component of micro push-out tests. Micro push-out testing directly measures properties of the interface, unlike in long fibre push-out testing, where fracture occurs locally and propagates along the interface, so debond stress as a material property is not directly measurable without assumptions or analytical adjustments.

Keywords: SiC composite, micromechanics, interphase, interface, fibres, Cohesive zone modelling

1. Introduction

Next generation fusion and fission reactors require high performance materials which are able to survive the high operating temperatures and high neutron irradiation doses predicted in operation [1]. Silicon carbide fibre-reinforced silicon carbide composites (SiC_f/SiC) are a leading candidate material for these applications. SiC_f/SiC is a class of ceramic matrix composite consisting of a complex architecture of SiC fibres within a SiC matrix and separated by a thin pyrolytic carbon interphase layer. The high strength of SiC_f/SiC is provided by the presence of nanocrystalline fibres and the transfer of stress from the matrix into these fibres via the interphase. Meanwhile, a weak interface within the interphase layer results in preferential cracking under load, triggering fracture energy consuming mechanisms such as crack deflection, fibre-bridging, fibre pull-out and micro-cracking. These give SiC_f/SiC its high fracture toughness via extrinsic toughening mechanisms (20-30 MPa $\sqrt{m}$ vs 4MPa $\sqrt{m}$ for monolithic SiC), although the onset of matrix cracking in microscopic tests remains close to the mode 1 fracture toughness of monolithic SiC [2, 3]. As described, the interphase plays a critical role in the unique properties of SiC_f/SiC and is a key enabler in the materials potential use for structural applications in nuclear environments.

Under high dose irradiation, the interphase of conventional nuclear-grade SiC_f/SiC composites can degrade due to the dimensional instability of residual carbon in SiC fibres and the pyrolytic carbon interphase which in extreme cases can lead to radiation-induced debonding between the fibre and matrix [4, 5]. Quantifying the mechanical effect of radiation damage at low and intermediate radiation doses is important for predicting lifetime performance.

The interfacial debond stress for mode II crack and interface friction of fibre-reinforced composites are critical parameters that determine the mechanical properties of components. Controlling these parameters during material design, and predicting its evolution in service requires scientific tools to measure and understand the fibre

*Corresponding author
Email address: alex.leide@ukaea.uk (Alex Leide)

debonding and sliding mechanisms. These tools should also be applicable to irradiated composites, necessitating a technique with minimal hands-on sample preparation for the case of radioactive material, and site-specific to minimize material test specimen dimensions and waste. The method should also apply to thin (<10 μm) layers to study ion-implanted samples, which are used to simulate the compositional changes from transmutation and accelerated displacement damage from the collision cascades caused by the incident ions.

Fibre push-out testing has been performed on both aerospace-grade composites with a BN interphase [6, 7, 8] and nuclear grades with a carbon interphase [9, 10, 11, 12, 13] to explore test parameters and variables. A novel in-SEM trench-based method has also been used to directly observe the failure mechanisms during push-out testing by FIB milling a trench underneath a vertically cross-sectioned fibre whereby SEM images can be acquired during the experiment [14]. Large scatter is typically found in these experiments due to microstructural variations such as porosity, fibre dimensions and position, and neighbouring fibres or matrix. The influence of experimental parameters has also been assessed, with recommendations that a flat punch tip with a diameter of approximately half the fibre diameter be used to avoid fracture or plastic deformation during the test while reducing the likelihood of mispositioning the tip over the fibre/matrix interface. The test success rate improves for thinner specimens, with thickness below 100 μm being recommended.

This paper presents results and a parametric study of a micromechanical method of short fibre push-out testing designed to study the interfacial debond stress of ion irradiated SiC_f/SiC composites. The experimental development is combined with finite element modelling to provide further insights into the mechanisms of fibre debonding and push-out. The modelling approach combines a cohesive zone model with Coulomb friction while accounting for radial stress caused by initial surface roughness and residual stresses [15, 11, 16]. A parametric study of Coulomb friction coefficients, the effect of rugosity on friction, the axial inclination of the fibres, and tapered fibre morphology are evaluated, and a detailed analysis is performed of three different fibres which were experimentally tested to validate results.

2. Methodology

2.1. Materials

The silicon carbide fibre reinforced silicon carbide matrix composite (SiC_f/SiC) used in this work consisted of Tyranno SA4 fibres (Ube Corporation, Japan) with a 90° 2D weave, an 80-100 nm thick pyrolytic carbon (PyC) interphase coating, and a SiC matrix both grown by chemical vapour infiltration followed by overcoating with SiC by chemical vapour deposition which resulted in a ~4 mm thick panel. This is a typical approach to manufacturing nuclear grade SiC_f/SiC composite.

2.2. Sample preparation

Specimens for ex-situ long fibre push-outs were prepared by cutting 20 × 4 × 0.6 mm thick cross-sections of the panel using a precision diamond saw, followed by thinning from both sides to ~180 μm using progressively finer diamond lapping films on an Allied Multimet precision polisher until final polishing with a 1 μm diamond lapping film, ensuring parallel faces. Actual thickness was measured using a Mitutoyo digital drop gauge. This thickness is within the recommended range from previous work. Specimens were mounted using Crystalbond mounting wax on polished 25 mm diameter pin stubs with slots laser milled into the surface in a grid pattern to receive the bottom of the fibre as it is pushed out.

Micro push-out specimens were cut from the same panel of SiC_f/SiC to dimensions 12 × 4 × 4 mm. These were ground and polished on four sides using diamond lapping films in the precision polisher to achieve a cuboid with parallel faces. Grinding with coarse films continued through the CVD coating to reveal fibre tows aligned parallel to the faces of the specimen. Final polishing was using 1 μm diamond lapping films. Trenches were focussed ion beam (FIB) milled to create the micro-push-out specimens with varying short gauge lengths. A combination of xenon plasma ion source (P-FIB Thermo Fisher Helios) and gallium liquid metal ion source (Ga-FIB FEI Helios 600) were used to create trenches. The surfaces of trenches were polished with low beam currents to create a smooth surface and minimize any milling artifacts such as preferential etching of the carbon interphase. This is shown schematically in Figure 1.

2.3. Push out testing

Ex-situ push-outs were performed using a 5 μm diameter diamond flat punch tip in an Agilent G200 nanoindenter with a displacement rate of 30 nm/s (see Appendix

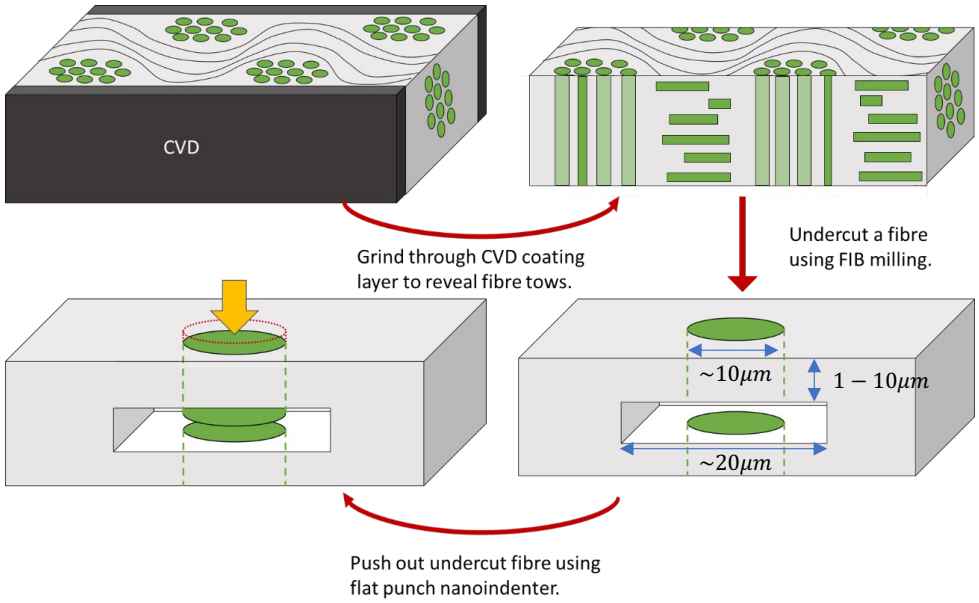

Figure 1: Schematic of preparing micro push-out specimens.

E). The instrument itself is inherently load-controlled with displacement rate determined by a feedback loop via capacitance measurements of displacement. The grid of slots in the pin-stub aided alignment of the tip to the fibres using the mechanical stage in the nanoindenter. Load-displacement data were recorded and used for analysis along with dimensions of the actual fibre measured by optical microscopy and post-test scanning electron microscope images acquired using a Tescan Mira FE-SEM.

Micro push-outs were performed in-situ using an Alemnis Standard Assembly inside a Tescan Mira SEM. A 5 μm diameter diamond flat punch tip was used for all tests. Displacement rates were either 100 nm/s or 10 nm/s. No effect of displacement rate was observed and 10 nm/s was used for the majority of tests. The Alemnis Standard Assembly fundamentally works in displacement control allowing measurement of load changes during the test, especially after fibre debonding. The frame compliance of the instrument is measured at 4.1 μm/N which causes ~90 nm displacement offset for the highest loads in the longest gauge lengths of these experiments.

2.4. Characterisation

Following micromechanical testing, selected push-outs were imaged and cross-sectioned using a FEI Helios 600 FIB-SEM and one push-out was sequentially milled using the slice and view method with 10 nm step size at 30 kV 0.12 nA. Platinum protective layers were deposited to protect the surface of all cross-sections. The slice and view images were reconstructed into a 3D dataset using ORS Dragonfly Pro software and segmented into "fibre", "PyC", "matrix", and "background" phases using U-Net Deep Learning algorithms trained by manually segmenting 7 slices of the dataset.

Raman spectroscopy mapping was used to measure residual stress around one of the fibres before and after the micro push-out experiment. Spectra were acquired using a Witec Alpha 300ARS with a 532 nm green laser operated at 25 mW focussed through a ×100 / 0.9NA objective lens to give ~1×1×1 μm signal volume. Depth resolution is estimated based on sub-surface depth profiles and is determined by the optical fibre acting as a confocal aperture between the microscope and detector optics. Maps were acquired with a 1 μm step size with 3s integration time for each step, and autofocusing using Witec True Surface. An 1800 g/mm diffraction grating was used to give 0.73 cm^{-1} spectral resolution, centred at 1200 cm^{-1} to incorporate the D and G bands of C-C bonding and the TO and LO Si-C vibrational modes. The spectrometer was calibrated using an internal sodium lamp and against a standard silicon reference sample before measurements took place. Further details of the data analysis procedure and residual stress conversions are shown in Appendix A.

2.5. Modelling

Push-out experiments produce mode II crack propagation in the PyC-fibre interface [16, 9]. A cohesive zone model (CZM) coupled with Coulomb friction has been

adopted to represent this failure behaviour. The cohesive zone model consists of a constitutive relation between the tractions acting on the interface and the corresponding interfacial separation. In the present work, we use a bilinear law as the constitutive relation [17].

A bilinear law can be divided into an elastic undamaged regime, damage-initiation criteria, a damage propagation regime and complete failure criteria. Constitutive equations in the undamaged regime are:

$$\begin{bmatrix} \sigma_n \\ \tau_s \\ \tau_t \end{bmatrix} = \begin{bmatrix} K_{nn} & K_{ns} & K_{nt} \\ K_{ns} & K_{ss} & K_{st} \\ K_{nt} & K_{st} & K_{tt} \end{bmatrix} \begin{bmatrix} \delta_n \\ \delta_s \\ \delta_t \end{bmatrix}, \tag{2.1}$$

where σ_n is the radial stress, τ_s and τ_t are the shear stress in the two tangential directions, δ_i is the opening displacement in the normal n or tangential directions t and s and K_{ij} are the stiffness matrix components which are K_{nn} = 2850 GPa/μm, K_{tt} = 1150 GPa/μm, K_{ss} = 1150 GPa/μm [18] and K_{ij}=0 GPa/μm when $i \neq j$ (uncoupled behaviour between shear and tension fracture modes).

Damage initiation is represented via the quadratic onset criterion:

$$\begin{aligned} &\sqrt{\left(\frac{\langle \sigma_n \rangle}{\sigma_I^{\max}}\right)^2 + \left(\frac{\tau_s}{\sigma_{II}^{\max}}\right)^2} = 1, \\ &\langle \sigma_n \rangle = \sigma_n; \ \sigma_n > 0, \\ &\langle \sigma_n \rangle = 0; \quad \sigma_n < 0, \end{aligned} \tag{2.2}$$

where σ_I^{max} and σ_{II}^{max} are the cohesive interface strengths for modes I and II (mode III is ignored for this model because the cylindrical shape makes it impossible since the fibres do not twist).

Once the cohesive damage has been initiated, the crack propagation regime begins. The interface resistance is affected by the damage caused by shear stress defined by the cohesive model and the friction (if $\sigma_n < 0$):

$$\begin{aligned} \sigma_n &= \begin{cases} (1-D)\bar{\sigma}_n; & \sigma_n > 0, \\ \bar{\sigma}_n; & \sigma_n \leq 0, \end{cases} \\ \tau_s &= \begin{cases} (1-D)\bar{\tau}_s; & \sigma_n > 0, \\ (1-D)\bar{\tau}_s + D\mu\bar{\sigma}_n; & \sigma_n \leq 0, \end{cases} \end{aligned} \tag{2.3}$$

where $\bar{\sigma}_n$ and $\bar{\tau}_s$ are the normal and shear components if the cohesive region were undamaged, in other words, defined by Equation (2.1), μ is the Coulomb friction coefficient. The contribution from the friction model is weighted by the cohesive damage variable D, which is 0 when the interface is undamaged and 1 when the failure is complete. The radial stress can be divided into two components $\sigma_n = \sigma_{nv} + \sigma_{no}$, σ_{nv} a variable component due to Poisson swelling of the fibre during push-out, and σ_{no} a constant component which corresponds to the sum of all the radial stresses. The radial stresses in the PyC interface are oriented in the radial direction of the fibre, its origin can be the rugosity of the interface, the difference between the thermal coefficient of fibre and matrix during the fabrication process, mechanical deformations, radiation etc [1]. In this work, a radial stress of σ_{no} = 420 MPa is imposed in the interface radial direction after an optimization process to adjust the friction after the failure of different fibres. If friction is calculated, $\tau_{friction} = \mu\sigma_n = \mu\sigma_{nv} + \mu\sigma_{no} = \mu\sigma_{nv} + \tau_0$ recovering the expression used in other push-out models [11, 19]. The complete failure is defined by the linear interaction criterion:

$$\frac{G_I}{G_{IC}} + \frac{G_{II}}{G_{IIC}} = 1, \tag{2.4}$$

where $G_I = \int \sigma_n d\delta_n$ and $G_{II} = \int \tau_s d\delta_n$ are the toughness values for mode I/II which are material properties obtained experimentally that represent the energy released when failure is complete. After complete failure, friction remains, being governed by Coulomb's law.

The FEM simulations were done by Abaqus 2021 software using C3D8 elements. It was used cohesive contact combined with tangential penalty friction [20].

3. Results

3.1. Fibre push-out testing

Conventional long-fibre push-out tests were performed to make a comparison with the micro push-out tests. Load-displacement curves for all the tests are shown in Figure 2. The curves show elastic loading, followed by small displacement jumps corresponding to crack initiation, propagation, fibre debonding, and a large displacement jump corresponding to the fibre being pushed out completely. Debond stress was calculated from the load at push-out divided by the interfacial surface area of the fibre, finding a mean debond stress of 59.5 ± 17.5 MPa (standard deviation) with a minimum value of 39 MPa and an upper value of 116 MPa. This simple assumption leads to an underestimation based on shear stress being uniform along the fibre length, which is not the case based on the modelling in [16] showing that the stress is localised near the surface and the crack propagates along the interface.

The fibre radius appears to affect the debonding stress, whereas smaller diameter fibres have a larger debond stress. This trend is most obvious for the long fibre push-outs in

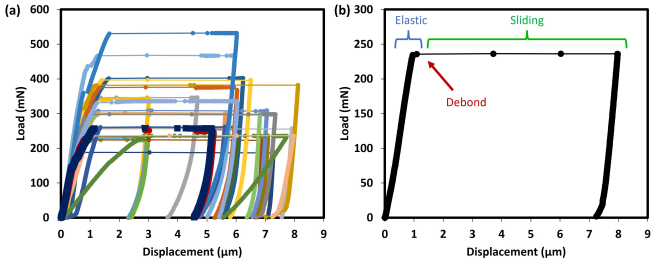

Figure 2: (a) Load displacement curves for all successful long fibre push-out tests. (b) single load-displacement curve labelled to show elastic loading, debonding, and frictional sliding.

Figure 3 (a) which are all tested in the same specimen with a thickness (gauge length) of 180 μm. Micro push-out data exhibit a greater range of debond stress, two abnormally large diameter fibres (~14 μm) present lower debond stress than expected according to the trend of gauge length shown in Figure 3 (c) having gauge lengths of 4.4 μm and 4.79 μm (fibres F5 and A4). Trendlines for debond stress are also plotted as a function of the fibre surface area and gauge length, showing a stronger correlation to the fibre surface area. This will be discussed later using Weibull fracture statistics. The micro push-out data points are also separated by their means of trench milling, whether by P-FIB or Ga-FIB or a combination. There was no clear trend of debond stress with the type of FIB used to prepare the push-out trenches.

3.2. Weibull analysis

The Weibull fracture theory is an established method to model fracture of ceramic materials based on failure occurring from the weakest part [21]. The average fracture strength τ_s for shear debonding of the interface can be expressed in Equation (3.1) as:

$$\tau_s = \int_{p=0}^{p=1} \tau dp = \int_0^{\infty} e^{-\int_S N(\tau) dS} d\tau, \tag{3.1}$$

where τ_s is the shear strength of the interface and p is the probability of fracture (both vary across the surface S of the interface due to different defects), $N(\tau)$ is a stress function that depends on shear stress τ on the interface caused by fibre push-out. Assuming only shear load on the interface $N(\tau)$ can be approximated to $N(\tau) = k\tau^m$, m is known as Weibull modulus and k is a constant for adjustment. The integral can be simplified to:

$$\tau_s = \int_0^{\infty} e^{-\int_S k\tau^m dS} d\tau = \frac{1}{(kS)^{1/m}} \int_0^{\infty} e^{-z^m} dz = C{\cdot}S^{-1/m}, \tag{3.2}$$

where the following approximations have been used:

$$\int_S k\tau^m dS = k\tau^m S = \left((kS)^{1/m}\tau\right)^m = z^m, \tag{3.3}$$

$$\int_0^{\infty} e^{-z^m} dz = \Gamma\left(\frac{m+1}{m}\right). \tag{3.4}$$

By plotting ln τ_s against ln S for micro push-out tests and conventional long fibre pushout tests, Figure 4 is obtained where the gradient is $-1/m$. For short fibres, $-1/m = -0.58$, giving a Weibull modulus, $m = 1.71$, with a coefficient of determination for this linear regression, $R^2 = 0.78$. For long fibres, $-1/m = -2.53$, giving a Weibull modulus, $m = 0.40$, with a coefficient of determination, $R^2 = 0.22$ signifying a poor fit. This linear analysis is similar to the exponential fit shown in Figure 3 (b) for short fibre tests.

3.3. Microstructural analysis

All push-out tests performed on this material responded by inside debonding where the fibre detaches from the interphase with the carbon interphase remaining attached to the matrix, similar to the observations in reference [12]. The surfaces on the underside of the pushed-out fibres did not have any carbon attached based on the cross-section images, showing that the crack had propagated completely along the inside surface, unlike in the case of BN interphases where the top of the fibre showed inside debonding and switched to outside debonding by the crack path deflecting through the BN midway along the trench [14]. This is consistent with the observations of solely inside debonding in push-out tests on similar nuclear grade SiC_f/SiC [9]. The slice and view imaging and 3D reconstruction in Figure 5 confirms that the PyC layer is continuous, remaining attached to the SiC matrix around the entire push-out with no observable cracking or co-extrusion of PyC as the fibre is pushed out.

The circular artefact which looks like an impression inside the fibre in Figure 5 is a result of uneven platinum deposition into the push-out impression leading to curtaining. No evidence of plastic deformation was seen on the surface of any fibres, and this curtaining artefact continues throughout the milling and appears in all slices - it is a results of FIB slicing rather than deformation from the mechanical test itself. Further images explaining the

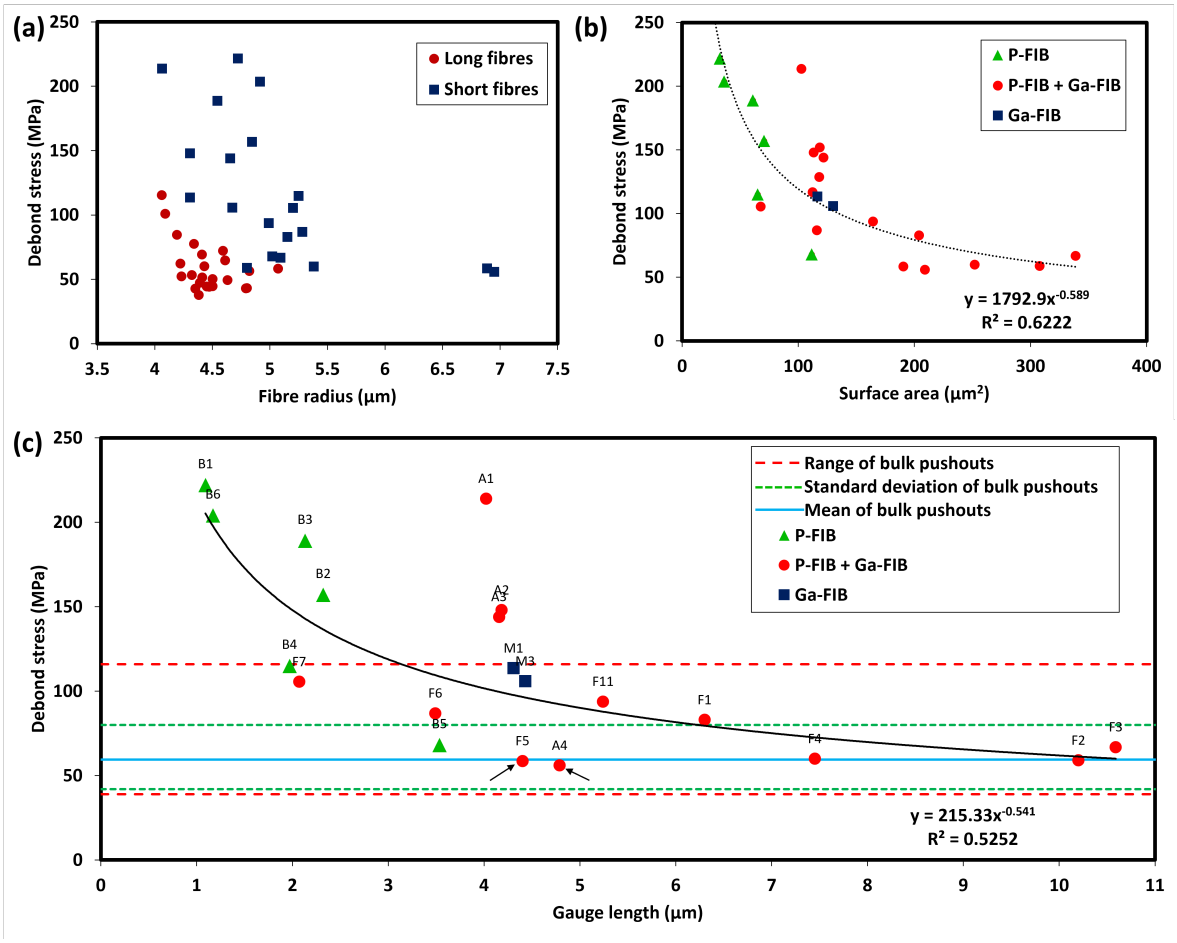

Figure 3: Debond stress as a function of (a) fibre radius, (b) fibre interfacial surface area, and (c) gauge length for micro push-outs. Horizontal lines in (c) indicate the range, standard deviation, and mean from long fibre push-out tests. Arrows in (c) indicate the tests with large radius fibres which are outliers in (a). Trend line equations and R^2 fitting values are shown in (b) and (c). Data point labels in (c) refer to the specific test IDs which will be referred to later.

origin of this artefact are shown in Appendix C. SiC is susceptible to significant redeposition, however, this is easily segmented and protects the bottom surface of the push-out during subsequent milling steps, preserving the PyC from preferential milling. Figure 5 (b) is a horizontal slice taken halfway through the remaining fibre within the matrix, indicated by arrows in (a). This shows cracks around the fibre, on the inside surface of the PyC layer, the most apparent of these are indicated with arrows. Rather than a continuous crack around the fibre in the reconstructed 2D plane, there appear to be many individual holes which correspond to the vertical scratched texture in the PyC highlighted in green in (a) and also shown in Figure 6 (a) and (d). No evidence of matrix cracking or crack deflection was observed in this 3D dataset.

The inner surface of the PyC adjacent to the fibres shows damage caused by the push-out process. Scratches parallel to the push-out direction are apparent in the PyC interphase caused by the surface of the fibres abrading the softer PyC, indicated by the white arrows in Figure 6 (a) and (d). The appearance of these scratches appears to be independent of whether the frictional component of the push-out test has a positive or negative gradient (Figure 6 (b) and (e)).

3.4. *FEA modelling of micro push-out experiments*

Three different fibre experiments have been fully modelled using finite element methods with variables adjusted until the simulated load-displacement curves matched the experimental load-displacement curves as closely as possible. The geometry has been approximated to a bridge with one fixed side in y direction, two fixed sizes in x direction and one free side, as depicted in Figure 7(a), given that three sides of the bridge are connected to the rest of the sample in the experiments while the other side remains unconnected after being milled to make a hole and create

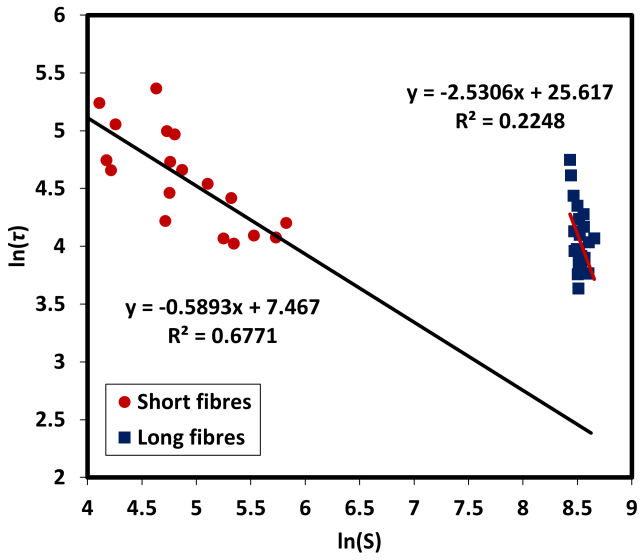

Figure 4: Weibull plot of micro push-out results with natural log of debond stress against natural log surface area showing good correlation.

the short fibre (see the experimental scheme on Figure 1). The load is applied to the top surface of the tip, being displacement-controlled. The geometry parameters of the different fibres are shown in Table 8 and the tip geometry is illustrated in Figure E.26(b).

The debond stress can be determined using the formula employed for short fibres [9] where F is the debonding force of the experiments, t is the thickness and R is the fibre radius:

$$\tau = \frac{F}{2\pi R t}. \tag{3.5}$$

The shear stress at the fibre-matrix interface in short fibres is considerably more homogeneous compared to that in long fibres, where damage initiation occurs gradually from the top to the bottom of the fibre. In short fibres, damage initiation occurs almost instantaneously across the entire contact interface, allowing for the application of Equation 3.5 (see Appendix H).

For the models, Young's modulus of the fibre and matrix, E_f = 365 GPa and E_M = 460 GPa, respectively, have been sourced from [22], and the Poisson's ratio is $\nu_m = \nu_f = 0.22$ [23].

Thus, the parameters to be optimized are toughness, the clamping stress attributable to surface roughness, and the Coulomb modulus. These parameters were adjusted using the procedure outlined in [16].

Friction Coulomb coefficient was fitted to μ= 0.15 (μ = 0.15-0.3), the clamping stress is σ_{no}=420 MPa, toughness to $G_I = 2.5\ \mathrm{J}/m^2$ ($G_I = 2.5 - 8.1\ \mathrm{J}/m^2$), $G_{II} = 10.5\ \mathrm{J}/m^2$ ($G_{II} = 10.5 - 34\ \mathrm{J}/m^2$), and the margins are obtained from [24, 18] except G_{II} calculated as $4.2 \cdot G_I$ [25]).

The toughness values are closer to the micropillar compression [24] where the area of the interface is smaller than the larger fibre push-out experiment. However, the G_{II} value is relatively high compared to similar materials such as SiC/BN/SiC, Gavalda-Diaz et al.[7] reported toughness values of $G_{II} = 1.2 - 3\ J/m^2$. Additionally, the criterion of $G_{II} = 4.2 \cdot G_I$ is based on fracture propagation in larger interfaces, where the anisotropy between mode I and mode II is less pronounced in the short fibres.

Several explanations have been proposed for this high value: First, Poisson swelling-induced radial stress may alter the fracture propagation resistance of the material [25]). Second, the roughness of the interface causes the fracture path to not follow a straight line, making propagation energetically less efficient [22, 16]. The roughness is considered when modelling friction see Equation 2.3, but not for fracture propagation. Third, there are different types of friction beyond Coulomb friction that may influence the crack when the sliding velocity is very low when crack is not completed.

In summary, G_{II} could be understood as the energetic work required for fracture propagation, which is a combination of interface toughness at a given pressure (σ_n), the energetic losses due to crack path, and certain friction terms at very low velocities (quasi-steady). The cohesive zone model separates the energetic contribution associated with Coulomb friction, which is predominant during fibre sliding, allowing for its quantification and distinction from other energy dissipation effects.

Finally, the mesh is defined based on the cohesive properties, as it is explained in full detail in Appendix G.

The Von Misses stress profiles of different micro push-out experiments F6, B2 and B4 are shown in Figures I.30, I.31 and I.32 of Appendix I respectively; brief explanations of the different effects are exposed below:

Fibre F6: Initially, the radial stress is applied before load (Figure I.30-1). When the load initiates, there is no crack and the structure presents an elastic behaviour, the Von Mises stress profile resembles that of a bridge undergoing bending with an applied load at the centre, resulting in a notable concentration of stress in the corners (Figure I.30-2). In particular, the interface exhibits the highest stress concentration on the bottom face, serving as the initiation point for crack formation [14]. After crack formation, there is a relaxation in the matrix deformation (Figure I.30-3), and the interface presents higher stress in

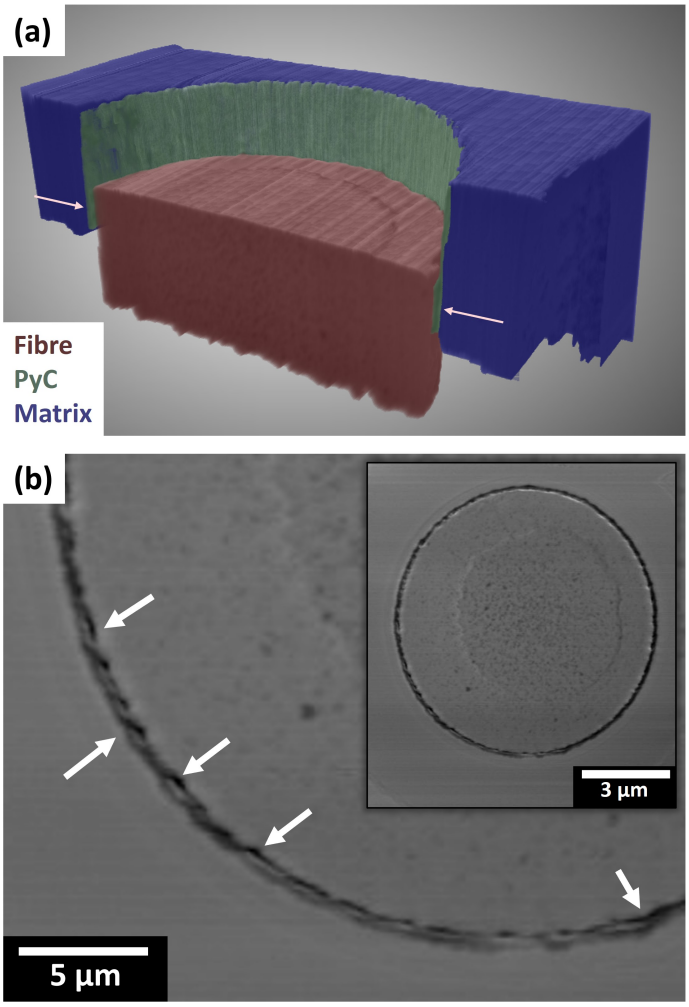

Figure 5: (a) Segmented and cropped 3D reconstruction with Pt cap and redeposition removed. A continuous layer of PyC remains attached to the matrix and is not observed on the pushed-out end of the fibre. (b) Horizontal slice through the pushed-out fibre reconstruction from the plane indicated by arrows in (a). White arrows guide the eye to cracks between the PyC and fibre, no cracks are observed between the matrix and PyC. The inset shows the full slice of the fibre in this plane.

the direction parallel to the z-axis. The asymmetric stress profile in the interface is due to the boundary conditions shown in Figure 7(a), where one of the bridge faces parallel to the y-axis is completely free while the other is fixed in the y-direction reproducing the geometry of the experiments. Regarding the fibre, the greatest deformation is observed in the centre of the fibre (see Figure I.30-4), indicating both bending and swelling. In the final stage, the fibre is predominantly pushed-out, and the matrix ceases to undergo bending, resulting in a homogeneous stress profile across the interface.

Fibre B4: The process is similar to fibre F6 featuring initial radial stress across the interface to represent the friction caused by rugosity (Figure I.32-1), an elastic response preceding the crack (Figure I.32-2), crack propagation (Figure I.32-3), and a post-crack frictional response (Figure I.32-4). The main difference with F6 is the faster propagation of the crack in the full interface. The low thickness allows more bending of the fibre, deforming the full interface instead of localized points in the bottom face, which propagates the crack to the top of the fibre.

Fibre B2: This fibre model was designed to investigate a real case of fibres with a positive-taper shape (the top surface of the fibre is bigger than the bottom one) and with axial misorientation (the fibre has an angle of inclination with respect to the indentation direction). The Von Mises stress profile before crack completion is akin to F6 and B4 push-outs (Figure I.31-1,2). After failure, the most significant difference lies in the order of magnitude of friction, while F6 and B4 reduce their frictional stress values while they are pushed out, B2 increases its frictional stress due to the positive-taper shape up to values bigger than the

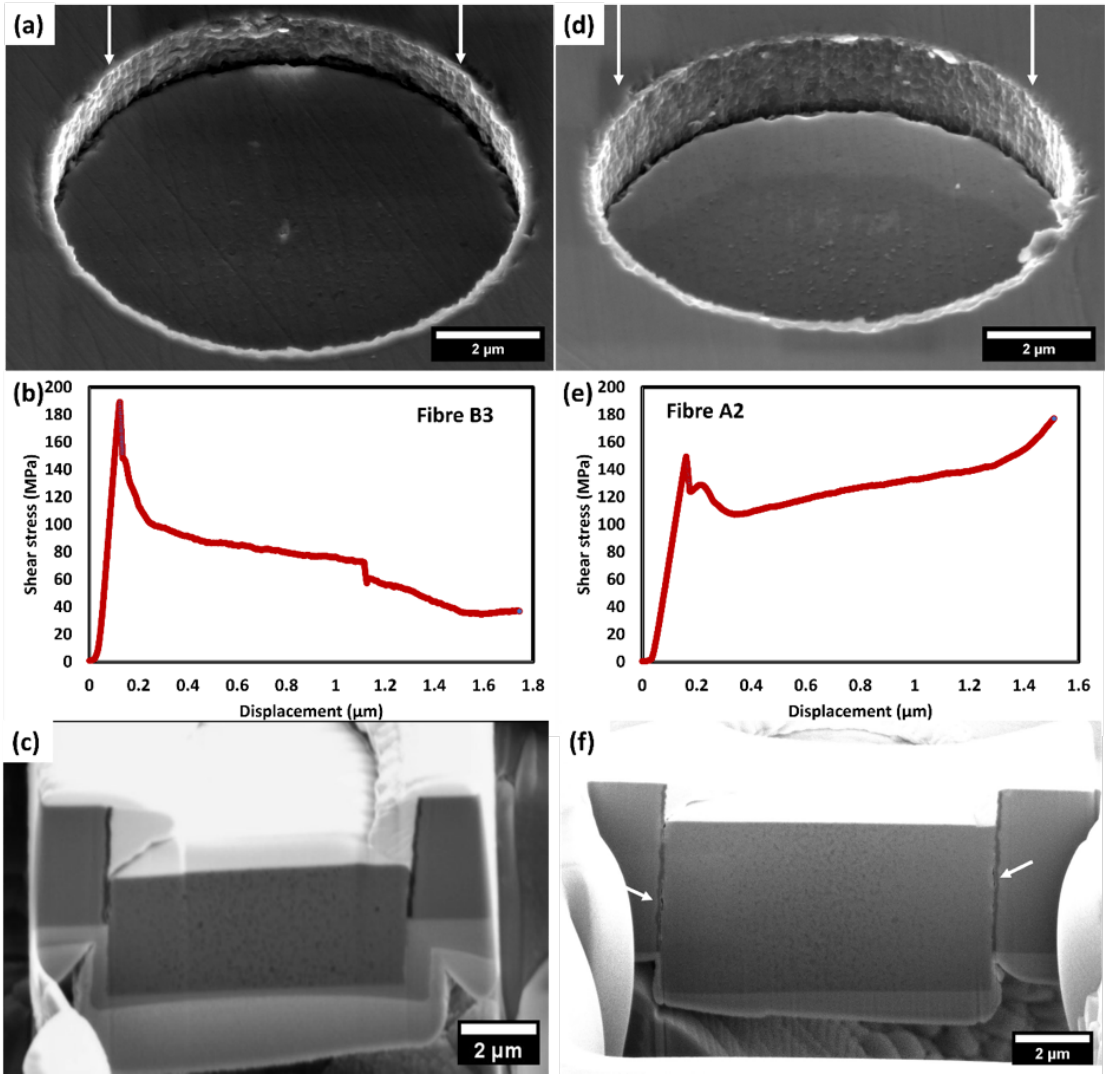

Figure 6: Post-test images of fibres B3 (a-c), and A2 (d-f) with their corresponding shear stress-displacement curves. (c) and (f) are FIB cross-sections of the pushed-out fibres, (c) taken from the slice and view imaging and (f) as a single slice.

peak stress before crack formation (see Figure I.31-3,4). Furthermore, the maximum stress concentration occurs on one side of the fibre, the reason is that an inclination of 8° creates an asymmetry in the friction. It is concluded that the axial misorientation and the taper shape are two important parameters that influence the push-out and they will be explored in detail in Subsections 3.6 and 3.7.

Finally, the force-displacement adjustments for different push-outs are shown in Figure 7 (b), models F6, B4 and B2 present small differences compared to the experimental data. The main difference occurs after the peak where the models fail to predict the small quasi-flat region illustrated in the experimental curves. This flat region could result from higher friction at lower velocities (something that occurs when the fibre's interface starts to crack), our models based on the finite element implicit method do not consider velocity effects. This effect occurs during the first 0.05-0.1 μm of the indenter's movement after crack formation having a reduced impact in the full push-out process (1.2-1.6 μm of displacement). The following presents a parametric study of the interfacial properties, followed by an analysis of the geometry (axial misorientation angle and taper shape of the fibre).

3.5. Parametric study – interfacial properties

In setting up the finite element models of fibre push-out, various intrinsic properties of the material can be adjusted as variables which are broadly unknown, or difficult to measure. The Fibre F6 push-out test served as the "original" and the finite element model of this fibre was adjusted to fit the experimental result as shown previously. The effect of adjusting each variable in the model

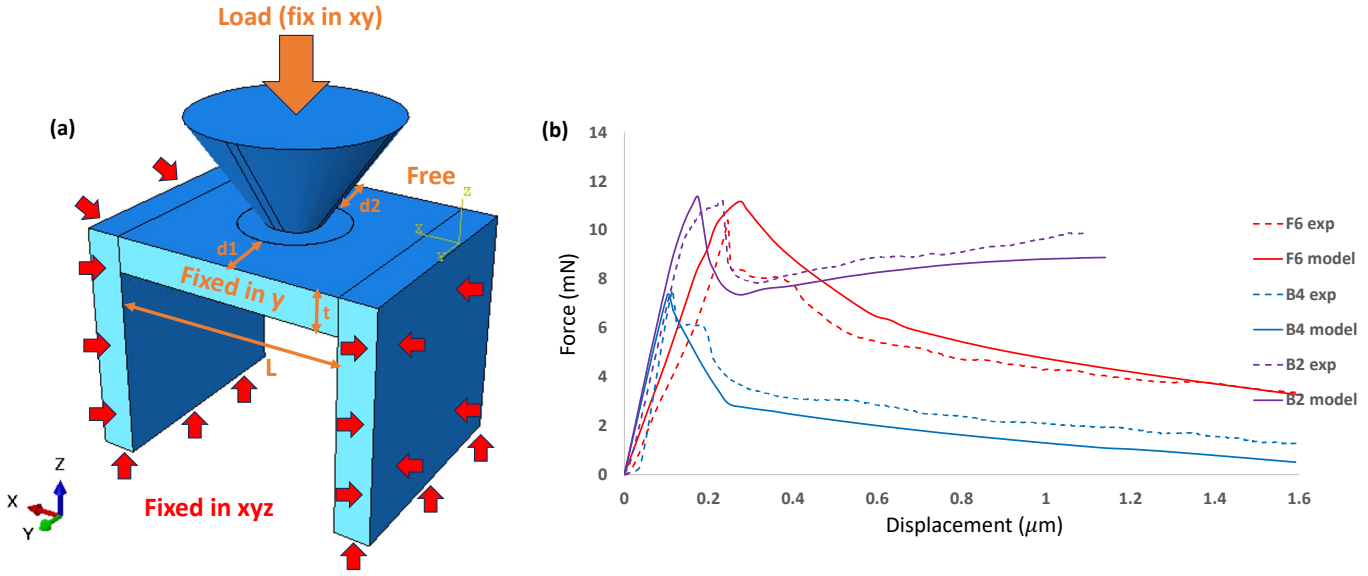

Figure 7: (a): Scheme of the geometry of push-out simulations. (b): Experimental and simulated load-displacement curves of three selected fibres.

Parameters	F6	B2	B4
L (μm)	22.50	23.00	21.00
t (μm)	3.49	2.32	1.97
d1 (μm)	5.97	10.33	17.01
d2 (μm)	5.97	20.00	17.01
Fib Diam top (μm)	10.56	9.67	10.50
Fib Diam bottom (μm)	10.56	9.60	10.50
Axial angle (°)	0	8	0

Figure 8: Table with the parameters for the geometry of the fibres F6, B2 and B4.

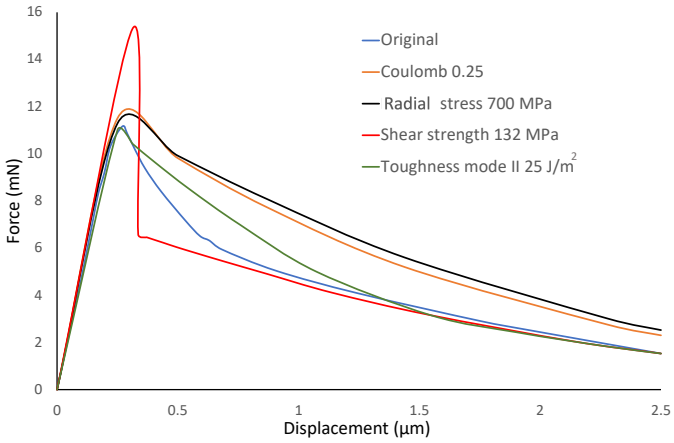

Figure 9: Effects of varying interfacial parameters.

away from the optimised version is demonstrated here to assign their relative importance and effect on the load-displacement properties of a micro push-out test. Figure 9 shows the effect of varying one parameter at a time, and these effects are summarised in Table 10.

Adjusting the debond stress of the interface of course increases the debond force, but causes a more rapid crack propagation while the frictional push-out component is unchanged. The faster crack propagation is due to the larger elastic energy release once the crack initiates, leading to faster propagation. Changes to the Coulomb friction coefficient and the radial stress are interchangeable as they are directly related to the frictional force. Increasing friction appears to increase debond stress, and slow crack propagation, extending the load drop, and of course, increasing the force for frictional sliding. Increasing Mode II toughness has no effect on the debond force or friction, but extends the crack propagation phase. Changes to Mode I properties have no discernible effect.

Of these interfacial properties, the most impactful to engineering properties is the frictional force which is caused by the Coulomb friction coefficient and the normal force which depends on the radial residual stress. This is a combination of surface roughness, chemical friction effects, and forces arising from residual stresses in the composite. Surface roughness is difficult to control; it is a property of the selected fibres, and chemical interactions on friction are determined by the material combination e.g. SiC sliding on PyC. Residual stresses are related to microstructure, manufacturing, and operating conditions and are expected to vary with operating temperature and

	Original	Modified	Qualitative Effect
Coulomb coefficient	0.15	0.25	Friction = Coulomb × normal force. Small increase in debond stress. Less sharp load drop. Increases friction throughout push-out.
Radial stress	420 MPa	700 MPa	Similar to Coulomb coefficient.
Debond stress (Mode II)	86.9 MPa	132 MPa	Increases debond stress. Friction unchanged
Mode II Toughness	10.5 J/m^2	25 J/m^2	Reduces load drop, but friction unchanged. Debond stress unchanged.
Tensile strength (Mode I)	86.9MPa	160MPa max and 1 MPa min	No changes to debond, crack propagation or friction.
Mode I Toughness	2.5 J/m^2	100 J/m^2	No changes to debond, crack propagation or friction.

Figure 10: Values for the parametric study.

radiation dose, and will be discussed later.

3.6. Parametric study – axial misorientation angle

Despite best efforts to align the specimen during preparation so that fibres are perpendicular to the surface of the specimen, it is impossible to achieve this in practice due to misorientation within fibre tows and the weaving angle of the 2D fabric. All fibres which were selected for undercutting appeared to have circular cross-sections on the surface which would indicate they are normal to the surface. FIB cross-sections of four fibres post-test reveal that these fibres are axially misoriented. The angle of misorientation θ of the cross-sectioned fibres is determined by measuring the angle of the interphase relative to the normal of the specimen surface and it is plotted with the debond stress in Figure 11. No significant effect of apparent misorientation angle on debond stress or sign (positive or negative slope) of friction component is observed for the range of angles experimentally measured here. The angle of the FIB cross-sectioning plane may impact the dimensions which are measured. All these axial angles and tapers (see below) are measured from single cross-sections except B3 which is determined from measurements throughout the 3D slice and view dataset.

An alternative approach to estimate the misorientation angle of a fibre is based on measuring the length of the two perpendicular radius of the faces with the highest difference in length. Assuming the fibre initially had a perfect cylindrical shape (circular faces), misorientation causes the fibre's face to become an ellipsoid (Figure B.22). In this case, the minimum radius represents the original fibre

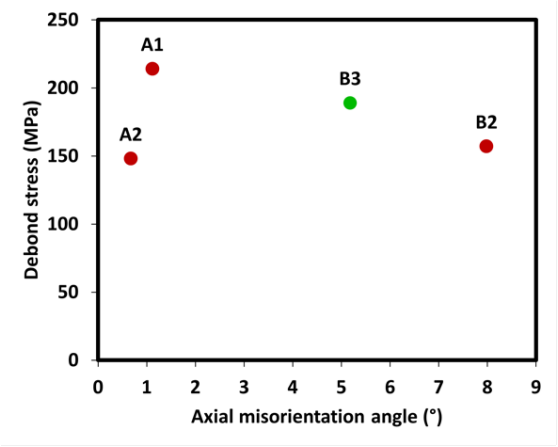

Figure 11: Effect of fibre misorientation angle on debond stress. B3 is highlighted in green as having a negative friction gradient (when the fibre is sliding, the force decreases with the displacement) whereas other tests have a positive gradient.

radius, and the maximum radius can be determined as:

$$r_{max} = \frac{r_{min}}{\cos(\theta)} \quad \Rightarrow \theta = \arccos\left(\frac{r_{min}}{r_{max}}\right). \tag{3.6}$$

To investigate the effect of misorientation angle further, a FE model for a prototypical fibre push-out is evaluated with varying misorientation angle up to a highly exaggerated 20°. The simulations have been conducted on a geometry as depicted in Figure 12, formed by a square of 22 μm of side, 7.45 μm gauge length and a fibre of 13.08 μm diameter where all sides of the matrix are fixed. In this case, the fibre has perfectly parallel sides. The parameters of the cohesive contact remain consistent with those outlined in Subsection 3.4, except for the interfacial

debond strength, which is set to 130 MPa. Inspecting the von Mises stress distribution of the fibre push-out model in Figure 12, there is stress localisation on the bottom of the matrix around the fibre, with a maximum on the acute angled side of the fibre and a minimum on the opposite side. This is related to the component of force normal to the interface applied by the push-out test.

Repeating these simulations across many axial misorientation angles with otherwise identical fibre characteristics shows an increase in maximum force for debonding, and very minor variation in the frictional sliding component of the test after complete interfacial debonding (Figure 13).

An analytical explanation of the increase in maximum force is provided by the geometry of the experiment, shown in Appendix B. In an ideal case, the equation for push-out force F in short fibres, where A is the fibre surface area and τ_B is the debond stress is simply:

$$F = \tau_B \cdot A. \tag{3.7}$$

The misorientation leads to an increase of interface area caused by a longer effective length of the fibre, t*. The change in fibre surface area with respect to the angle can be written as:

$$A = 2\pi r \cdot \frac{t}{\cos\theta}. \tag{3.8}$$

The component of force acting to push-out the fibre is simply $F \cdot \cos\theta$. Combining these equations, the force required to debond and push-out a fibre from a matrix is:

$$F = \tau_B \cdot 2\pi r \cdot \frac{t}{(\cos\theta)^2}. \tag{3.9}$$

However, this analytical expression (Equation (3.9)) based on simple geometry does not provide sufficient correction in debond force compared to the FEA simulations, suggesting a change in the fibre push-out mechanisms with increasing angle (see Figure 14). The initial discrepancy at small angles is related to the assumption that force is uniform in the fibre for the analytical approximation and that debonding occurs instantaneously along the interface. In this geometric adjustment, the interface-normal components of force are assumed to cancel out, i.e. the compressive force on one side is balanced by the tensile force opposite. This assumption is applicable in the frictional sliding portion of the experiment, as shown by the small variation in this part of the curves in Figure 13; however, the initiation of debonding is a fracture mechanics process where a tensile component is not equivalent to a compressive component.

With increasing misorientation, the force propagation of the push-out will cause a tensile and a compressive load on the opposite sides of the fibre (Figure B.22), decreasing and increasing the friction respectively when the microcracks are formed and altering the crack propagation. A complete demonstration of this is shown in Appendix B, showing the different crack propagation from the compressed and the tensile side. Despite these differences in crack initiation and propagation mechanisms, the variation in the debond force with the angle of misorientation is small compared to other experimental effects, and the change in push-out friction is minimal. Therefore, the model parameters adjustment shown in Figure 7 can be valid even if the fibres were slightly misoriented.

3.7. Parametric study – taper

The effect of fibre taper on debond stress and pushout friction gradient for the same four cross-sectioned fibres is shown in Figure 15. In this case, the value for taper is the average angle of the sides of the fibre. This is calculated from $tan^{-1}(\frac{r_{\text{top}} - r_{\text{bottom}}}{L})$ where r_{top} is half the measured width at the top of a fibre and r_{bottom} is half the measured width at the bottom of a fibre, and L is the gauge length of the fibre measured from cross-sections made at approximately the diametric plane of the fibre. Negative angles are referred to as negative taper, and positive angles are referred to as positive taper. Fibre B3, which has the most prominent negative taper measured from the FIB cross-section, is the only test with a negative friction gradient following debonding, as shown in Figure 6 (b). In the cross-sectioned plane, fibre A2 has a slightly negative taper, however, the mechanical response during the test gives a positive friction gradient shown in Figure 6 (e), while the fibres A1 and B2 which have measurable positive taper also have positive friction gradients. Based on experimental results in Figure 15, fibre taper appears to have no discernible effect on debond stress, i.e. the peak force in the experiment; fibre B3 with large negative taper has similar debond stress to the other fibres. The taper does appear to have a large effect on the gradient of the shear stress component after debonding; fibre B3 has a negative gradient showing decreasing shear stress during pushout whereas the other fibres have a positive gradient even when displacement is taken into account in the shear stress calculation.

To investigate the taper effect further, FEA simulations were implemented in Abaqus using axisymmetric CAX4 elements. In these models, the fibre is 4 μm long with 4 μm maximum radius at the top of the fibre, while the radius

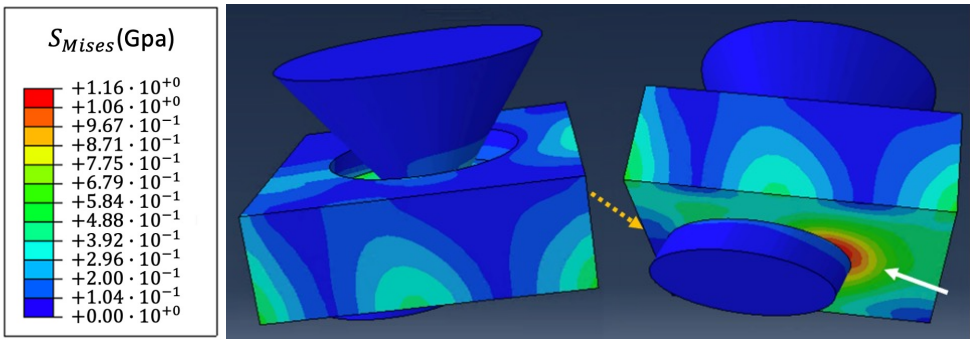

Figure 12: FEA simulation of fibre with exaggerated axial angle of 20 degrees. Solid white arrow indicates stress maximum on the bottom of the matrix on the acute angled interface. Orange dashed arrow indicates a stress minimum on the opposite side of the matrix.

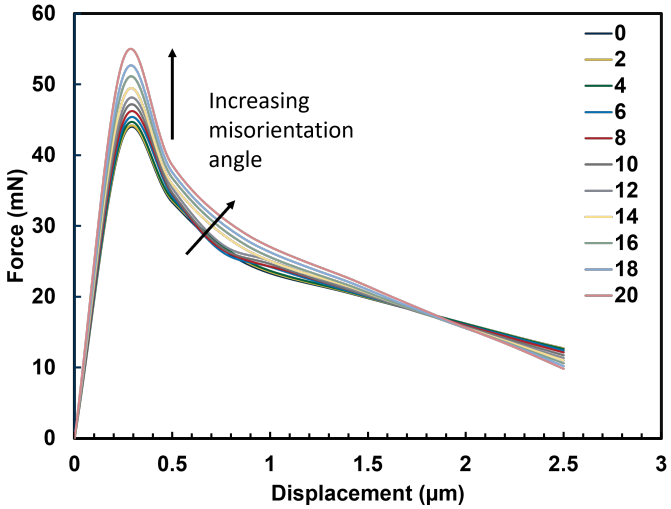

Figure 13: Effect of misorientation angle on load-displacement curves between 0 and 20°.

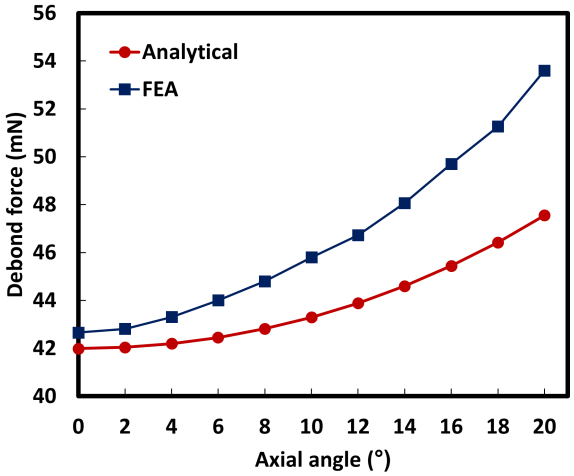

Figure 14: Effect of axial angle on debond force comparing FEA and analytical approximations.

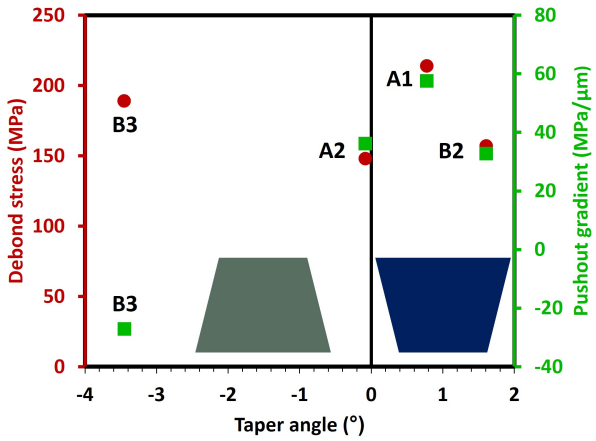

Figure 15: Effect of fibre taper on debond stress (red circles) and pushout gradient (green squares). B3 has a negative friction gradient during push-out. Definitions of negative and positive taper are indicated by the shapes.

at the bottom varies from 4 to 3.6 μm, corresponding to a range of fibre taper angles from 0° to 9.93°. The debond stress was set to a high value τ_s = 300 MPa to appreciate the load drop compared with the load increase caused by the taper effect, no radial stress was applied to clearly differentiate the effect of fibre taper compared to other causes of friction (roughness, thermal stress or defects). The remaining cohesive properties are the same as the fibres modelled during the experimental simulations (Toughness G_I = 2.5 J/m^2, G_{II} = 10.5 J/m^2 and Coulomb friction μ = 0.15). This is a simplified case to isolate the role of fibre taper - an analysis of taper combined with friction follows beneath.

Figure 16 shows horizontal (σ_{rr}) and vertical (σ_{zz}) and von Mises stress profiles in the cross-sectional plane during early stages of frictional push-out of simulations of a parallel and positively tapered fibre. Key to note is the

larger stress at the interface in the tapered fibre case, where σ_{zz} is nearly homogeneous across the full interface and σ_{rr} varies across fiber length being the fibre compressed on the top (σ_{rr} has $-r$ direction) and expanding the matrix hole in the bottom of the fiber ($+r$ direction). The much higher load for tapered fibres causes larger stresses within the fibre, clearly shown in the von Mises stress profile in Figure 16 (f).

Force-displacement profiles for the simplified parametric study of various fibre tapers show that debond force is not affected, in agreement with the experimental results, but the crack propagation and frictional stage are significantly altered (Figure 17). The compressive interfacial forces identified for the tapered simulation in Figure 16 are induced following crack initiation, and oppose the interfacial crack propagation effectively increasing the toughness and slowing crack propagation, so the load drop is smaller and over a larger displacement between the initial debonding and the frictional sliding portions of the test. For the perfectly parallel fibre with 0 taper, the friction component falls to 0 force and remains at 0 with a very short crack propagation stage as expected for this simplified case with no radial force, only the cohesive properties applied to the interface. With increasing misfit of the fibre in the matrix hole, the force to continue push-out increases and can exceed the debonding force, as observed experimentally.

The analysis of friction combined with fibre geometry has been studied using shear lag theory [16, 26], the force due to friction resistance P_{fric} with respect to push-out displacement (u) is defined through the expression:

$$P_{\text{fric}} = C_{\text{Diff}} \frac{A_{\text{top}}\, E_{\text{fibre}}}{v_{\text{fibre}}\, R(u)} \left[\exp\left(\frac{2\mu\Lambda v_{\text{fibre}}\,(t-u)}{(R(u) E_{\text{fibre}})} \right) - 1 \right],$$
$$\text{where} \quad \Lambda = \frac{E_{\text{fibre}}\, E_{\text{Matrix}}}{E_{\text{Matrix}}\,(1-v_{\text{fibre}}) + E_{\text{fibre}}\,(1+v_{\text{Matrix}})}. \tag{3.10}$$

C_{Diff} is an amplitude term, $R(u)$ is the radius of the deformed fibre and L_{fibre} is the length of the fibre.

Equation (3.10) can be modified for fibre taper by substituting the amplitude term $C_{Diff} = k \cdot u$. Where $k = (R_{\text{max}} - R_{\text{min}})/L_{\text{fibre}}$ represents the geometry of the taper for a push-out displacement of u (R_{max} and R_{min} represent the value of the radius at the top and bottom of the fibre respectively). The taper effect also modifies $R(u)$ as the radius of the deformed fibre, which is replaced by $R(u) = R_{max} - k \cdot u$. The area of the top face of the fibre is $A_{top} = \pi R_{max}^2$, E_{fibre} and ν_{fibre} are Young's modulus and Poisson ratio of the fibre, μ is the friction Coulomb coefficient, E_{matrix} and ν_{matrix} are Young's modulus and Poisson ratio of the matrix and t is the thickness of the sample/length of the fibre.

$$P_{\text{fric}} = \frac{k \cdot u \cdot A_{\text{top}}\, E_{\text{fibre}}}{(R_{\text{max}} - k \cdot u) \cdot v_{\text{fibre}}} \left[\exp\left(\frac{2\mu\Lambda v_{\text{fibre}}\,(t-u)}{((R_{\text{max}} - k \cdot u)\, E_{\text{fibre}})} \right) - 1 \right]. \tag{3.11}$$

Equation (3.11) does not consider the debond strength or toughness, just the friction post-cracking. In Figure 18 this theoretical model is compared to the FEM simulation of fibre push-out including friction components with and without interfacial bonding for a 3.9 μm bottom radius and 4 μm top radius positively tapered fibre. During fibre sliding, there is an initial increase in force due to the taper effect, then a force peak and drop as the surface area of the fibre-matrix interface and therefore frictional force is reducing, There is a good match between Equation (3.11) and the finite element model beyond push-out, showing the potential applicability of this equation. Importantly, the friction component is identical whether there is an interface bond or not – this indicates that the modification to friction caused by the taper effect is not linked to the interfacial debond stress of a fibre and that the debond stress is still a valid property when experimentally measured from a tapered fibre.

Fibre taper has no apparent effect on debond stress but dominates the frictional push-out component of the test. The variation of the diameter along the fibre axis has previously been shown to have a significant effect on increasing the friction during the push-outs of longer fibres (approx. 50-100 um long), which results in higher sliding force after the crack is completed [16, 26]. However, this force never exceeds the debond force in long fibres, contradicting some short-fibre experiments where the frictional force was greater than the debond force, having short fibres a higher debond stress than long fibres. The explanation is that in longer fibres there are regions with negative tapered shapes compensating the friction produced by the positive tapered regions.

3.8. Raman spectroscopy residual stress measurements

Raman spectroscopy maps were acquired around the area of test A3 before and after push-out testing. By segmenting fibre pixels from matrix pixels using principal component analysis, and further segmenting the specific push-out fibre and local matrix, spatially averaged spectra are acquired shown in Figure 19 (c). Before push-out, the fibre has a characteristic TO peak at 796 cm^{-1} which moves to a higher wavenumber of 799 cm^{-1} after push-out. 796 cm^{-1} is commonly reported as the stress-free

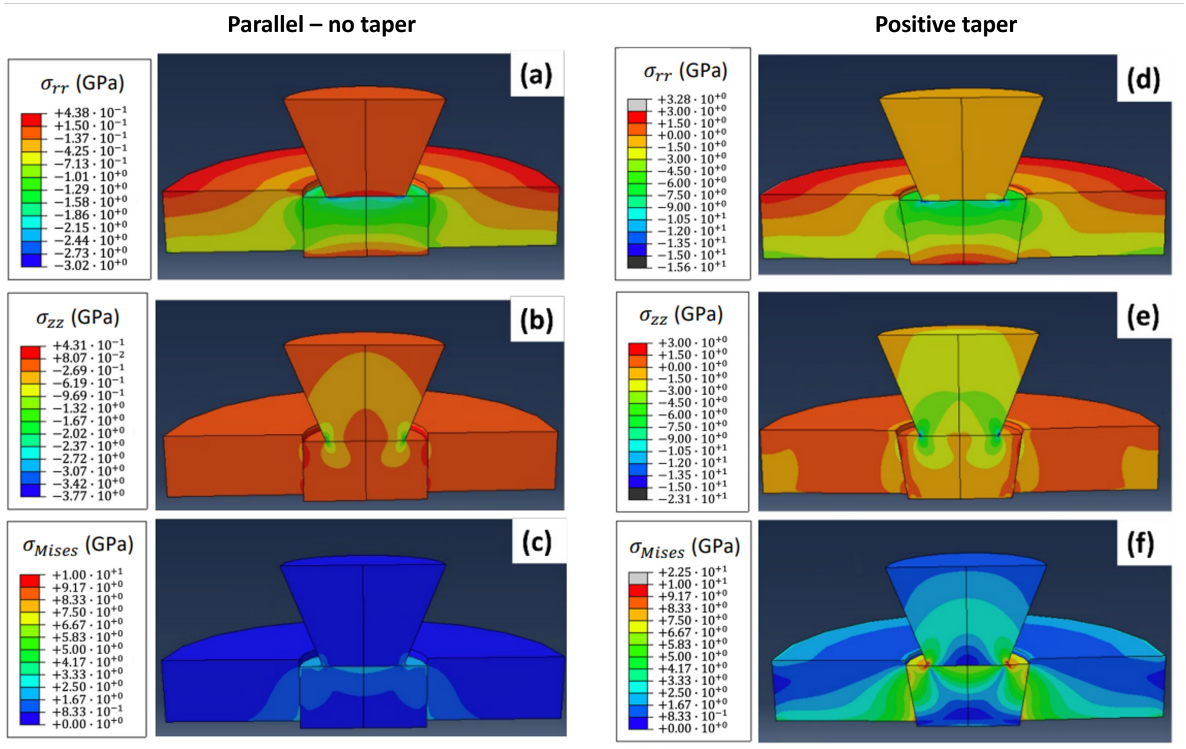

Figure 16: σ_{rr}, σ_{zz}, and von Mises stress distributions for pushed-out fibres during the frictional sliding phase for (a)-(c) parallel-sided fibre and (d)-(e) positively tapered fibre. Note the ~10x larger colour scale for the tapered fibre σ_{rr} and σ_{zz} components, while von Mises stress is on the same colour scale. All stresses are in MPa.

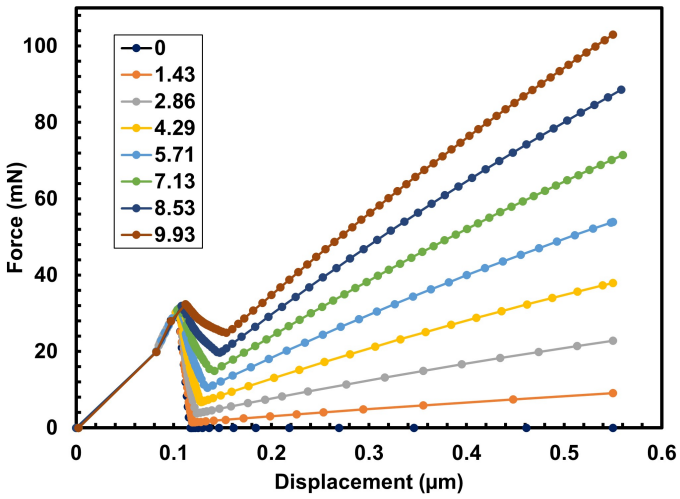

Figure 17: Force-displacement curves for a simplified fibre push-out test with varying extents of positive taper in the absence of a radial stress. Each line corresponds to increasing fibre surface angle, each with the bottom radius decreasing by 0.1μm .

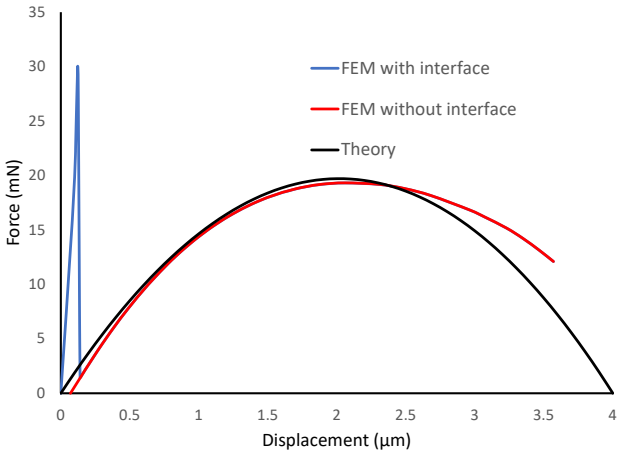

Figure 18: Comparison of modified shear-lag theory with FEM for a positively tapered fibre. The force-displacement behaviour of FEM with the interface (the fracture of a cohesive interface separates the fibre from the matrix previous to friction) matches with the FEM without an interface (only friction provides resistance to fibre sliding) except for the initial peak that corresponds to the interface crack.

value of 3C-SiC [27]. Shifts to higher wavenumbers indicate relative compressive elastic strains on the Si-C bonds. Tyranno SA4 fibres contain pockets of free carbon which are distributed within the fibre microstructure. The stress-free position for the carbon G-band peak is 1580 cm^{-1} and is the one used for stress analysis with the conversion factor

derived by Frank et al. [28]. Averaged across the fibre, the peak position is at 1594 cm^{-1} before push-out indicating a large compressive residual stress in the carbon pockets of the fibres relative to an un-stressed planar carbon. Following push-out this moves to 1598 cm^{-1} indicating a further increase in compressive stress on the carbon pockets of the fibres.

The TO peak of the matrix is at much lower wavenumbers compared to the fibre; being at 787 cm^{-1} before push-out, and 788 cm^{-1} after push-out which is more characteristic of 6H-SiC, along with smaller peaks at 799 cm^{-1} and 767 cm^{-1} [27]. This may be due to the high density of stacking faults in low-temperature deposited CVI SiC which locally causes hexagonal stacking in a cubic grain. The higher relative scattering intensity of the 6H-SiC TO peaks compared to 3C-SiC TO peaks could explain this spectrum being from a combinaiton of 3C and 6H scattering. With the spectral resolution of the equipment used here, the 799 cm^{-1} signal from 6H-SiC should be a distinct peak rather than a shoulder, further suggesting that it is a combination of the signal from 3C-SiC and 6H-SiC. Assuming that the elastic stress on the stacking faults in CVI SiC is equivalent to the stress on the cubic phase, it may be simpler to use the more easily identifiable 6H-SiC peak position as the stress-free reference. Considering the stress-free TO peak position of 6H-SiC is at 789 cm^{-1}, this suggests a slightly tensile stress in the SiC matrix around the fibre prior to push-out. After push-out, the peak position moves closer to the stress-free peak position indicating stress relaxation in the near-surface matrix around the residual hole left by the fibre push-out test, while remaining in residual tension relative to a stress-free 6H reference. The shear stress-displacement curve in Figure 19 (d) shows a slight upward gradient followed by a steep upward gradient during the frictional sliding component of the push-out test. This indicates that the friction component is increasing which may be caused by a positively tapered fibre pushing into a narrower hole. The steeper increase in shear stress at larger displacements may be caused by an increasingly positive taper of the fibre, or the bottom of the fibre hitting redeposited material at the bottom of the trench; during the in-SEM tests, the tip did not visibly contact the edge of the trench and no damage was observed around the pushed out fibre which could be attributed to the indenter tip contacting the matrix and causing the load increase.

4. Discussion

4.1. Considerations for micro push-out testing

The purpose of developing micromechanical methods, including this micro push-out technique is to be able to acquire useful mechanical data using small-scale specimens. In the specific case of nuclear materials, the key requirement is to extract mechanical data from shallow ion-irradiated layers which are created while implanting transmutation elements or when using ions to accelerate displacement damage. Typically, ion irradiation facilities operate at up to 5 MV accelerating voltage which, depending on ion species, charge stage, and experimental design, can generate damage depths between 0.5 μm - 10 μm in SiC. Lighter ion species, or multiply charged heavy ions can penetrate to deeper depths.

For general post-irradiation characterisation, at least 1 - 2 μm ion irradiated is preferred, where larger depths can more effectively decouple substrate effects from the measured properties in the thin layer [29, 30]. The results in this work suggest that a gauge length greater than ~4.5 μm is suitable for assessing bulk mechanical properties, which is within the range of radiation damage depths achievable with ion irradiation (see Figures 3 (b,c)). At this point, the fibres essentially become "long" with a reasonable concentration of interface defects. An upper limit of gauge length (or interface surface area) will occur when there is non-uniform stress on the interface, there is too much fibre swelling, and there is stable crack growth leading to friction effects. While not the purpose of the work, in the appendix of reference [16] a simulated fibre with length <15 μm had uniform surface stress while longer fibres experienced stable crack growth. Further work may be required to determine this inflection point of push-out mechanisms, however it appears that this will be at longer lengths than achievable in ion irradiated layers.

Interfacial failure in micro fibre push-out tests of SiC_f/SiC composites appears to be statistical, based on Weibull distributions of defects, therefore, interface surface area is the more specific parameter to be assessing against, as shown in Figure 3 (b). The trend of debond stress with interfacial area shows that interfacial areas greater than ~160 μm^2 are representative of long fibre push-out tests. Considering that apparent fibre diameter can easily be measured on the surface of the specimen, when preparing trenches for micro push-out tests a general rule for determining the required gauge length for a test can be written as:

$$L_f > \frac{160}{2\pi r}, \tag{4.1}$$

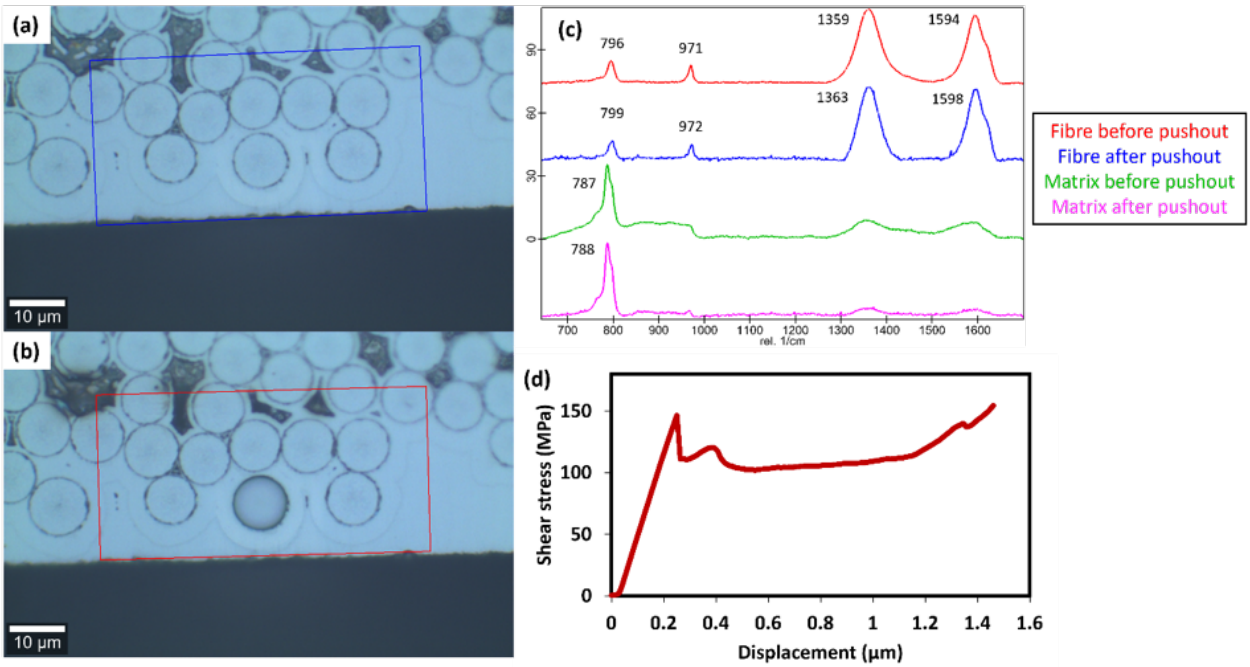

Figure 19: Optical micrographs of push-out A3 (a) before and (b) after testing along with (c) averaged Raman spectra for the individual fibre before and after push-out (red and blue curves) with the average spectra for the CVI matrix before and after push-out (green and pink curves). (d) shows the stress-displacement plot for this push-out test.

where L_f is gauge length and r is the fibre radius in microns. This relationship is important as the micro push-out tests can only be performed on the edge of a sample where a trench can be milled into the side of the specimen to undercut a fibre, and the position of the trench has to be set by the user for each specific test rather than by bulk parallel thinning of a specimen. Being limited to the edge of a specimen also severely limits the options for testing fibres compared to a bulk push-out test where there are many suitable fibres within a specimen, therefore it is important to ensure that those tests are successful, also considering the high cost of FIB micromachining compared to mechanical thinning.

When debond stress is plotted against gauge length, and to a lesser extent interfacial surface area (Figure 3 (b) and (c)), it is appears that xenon P-FIB milling could enable shorter gauge lengths to be tested than trenches prepared using Ga-FIB or with final polishing using Ga-FIB. While this was not a specific parameter for analysis in this study (choice was dependent on instrument availability), it may be a consideration for future experiments. As gauge lengths become shorter, surface damage has a relatively stronger effect, therefore FIB damage may not be negligible. Xenon ions are heavier than gallium ions and penetrate to shallower depths at 30 kV accelerating voltage, causing less damage to the surfaces of the push-out specimen, whether during FIB imaging on the surface during sample alignments or during undercut milling and polishing.

The Weibull modulus, m=1.71 which was calculated for the debonding stress in micro push-out tests in this work is rather low compared to literature values for thick pyrolytic carbon materials reported in the literature to be between m = 8 and m = 11 [31]. This statistical analysis suggests that critical flaws leading to failure are not associated with pyrolytic carbon but with the fibre-PyC interface, which agrees with the microstructural observations for inside debonding of the fibre-matrix interfaces in this work and the literature [9, 22]. The debonding mechanism is associated with flaws on the surface of the fibre which is likely to be a function of surface roughness and interphase deposition conditions rather than an intrinsic property of PyC itself.

Although we have defined an approximate size cut-off for micro push-out testing to be representative of bulk push-out testing, Weibull statistics could be applied to extrapolate smaller scale testing to larger length scales using a volume or area adjustment. The probability of failure Weibull plot $lnln(\frac{1}{1-P_f})$ vs $ln(\tau_s)$ for the short and long fibre experiments is shown in Figure 20 with straight lines fitted to the straight portions of the data, ignoring low strength outliers. The gradient of fitted straight lines in

Figure 20 gives the Weibull modulus as $m = 1.90$ for short fibres and $m = 2.54$ for long fibres with $R^2 = 0.97$ and $R^2 = 0.93$ respectively. For short fibres, this is a close match to the method in the Weibull analysis section following the derivation in [21] based on a weakest link model ($m = 1.71$ and $R^2 = 0.78$), the difference is that an average surface area is used in the probability of failure method. However, for long fibres there is a significant difference ($m = 0.40$ and $R^2 = 0.22$) in the Weibull modulus calculated by each method, indicating that long fibre push-out testing does not follow a Weibull theory of failure from the largest defect in a tested volume [32]. The non-Weibull failure mechanism for long fibres is also apparent based on the very poor fitting in Figure 4, the reason for long fibre testing being non-Weibullian will be discussed. Extrapolation of the short fibre fitted line to long fibre surface area ($ln(S) = 8.5$) in Figure 4 gives an approximate debond stress $\tau_s = 11.7$ MPa, significantly lower than the values measured in long fibre experiments. Micro push-out testing therefore, follows a Weibull distribution for interfacial debond stress but long fibre push-out testing does not.

As a more general approach, where micro push-out experiments have been conducted with approximately the same gauge length and surface area, as might be the case during post-irradiation examination of an ion-irradiated specimen, the probability of failure method becomes more appropriate than comparing τ_s with the surface area. To extrapolate to long fibres, Equation 4.2 shows the relationship between a stress τ and surface area S to relate specimens with different effective sizes *via* the Weibull modulus, m.

$$\frac{\tau_{long}}{\tau_{short}} = \left(\frac{S_{short}}{S_{long}}\right)^{\frac{1}{m}} \tag{4.2}$$

As an example, we will use the data collected in this work to relate small specimen experimental data to large specimen sizes using this relationship. The short fibre push-outs are intentionally across a range of gauge lengths for the parametric study which is not the optimal approach for a Weibull analysis based on the probability of failure approach, but will serve the purpose for this demonstration.

Using the characteristic strength of short fibres, i.e. the debond stress from the $lnln(1/(1-P_f)) = 0$ intercept which corresponds to P_f=63.2% gives $\tau_{short} = \exp(4.9) =$ 132 MPa. The average surface areas ignoring low-strength outliers from Figure 20 for short (115 μm^2) and long fibre tests (5010 μm^2) are used to represent the measurement size in Equation 4.2. The Weibull modulus of short fibres ($m = 1.90$) is used in this case to give an estimated

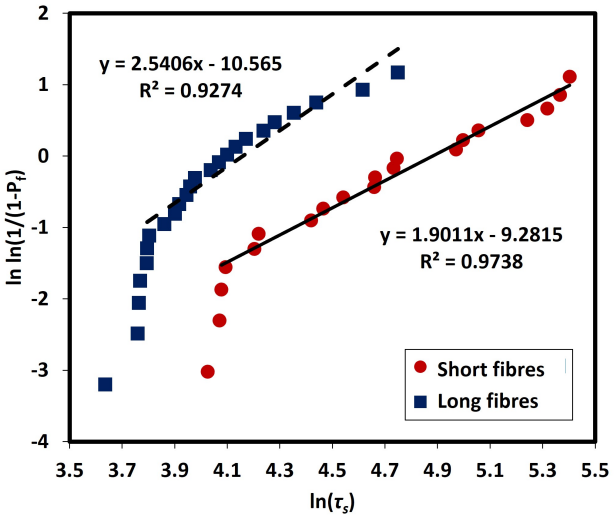

Figure 20: Weibull probability of failure plots $lnln(\frac{1}{1-P_f})$ vs $ln(\tau_s)$ for long and short fibres from this work. Straight lines are fitted ignoring the low strength outliers in each dataset.

characteristic strength of long fibres calculated from short fibre data as $\tau_{long} = 18.1$ MPa employing the size effect relationship in Equation 4.2 being significantly different from the values obtained by long fibres push-outs. The explanation of these differences between long and short fibres (in the Weibull coefficients m and the debond stress τ_s predicted compared to the measured) comes from the fracture propagation process. In short fibres the stress over the interface is pretty homogeneous, while in long fibre the fracture process is gradual, initiating in the top and propagating to the bottom. In reference [16], the stress profile of a long fibre push-out is modelled, having the bottom of the interface undamaged while the top is completely broken. Furthermore, the extra resistance of the undamaged interface causes additional Poisson swelling which increases its effect on fracture propagation. These different mechanisms mean that the interfacial shear stresses (force per interface surface area) from long and short fibre pushout techniques are not comparable and one cannot be directly extrapolated from the other. Within the regime of "short fibre" testing, different size tests are comparable using Weibull analysis.

The long fibre push-out tests in this work are comparable to literature data on fibre push-out testing of nuclear grade SiC_f/SiC composites with PyC interphases and modern fibres. The interfacial debond stress (obtained from Equation (3.5)) was 59.5 ± 17.5 MPa, close to the 69.4 ± 14.4 MPa measured by Hussey *et al.* using Tyranno SA3 fibres with PyC interphase and CVI SiC matrix, a

very similar material to our work [9]. Buet *et al.* studied a variety of composites and compared fibre-matrix interfacial mechanical properties of samples made using Hi-Nicalon Type-S and Tyranno SA3 fibres with different PyC interphase textures and thicknesses in a CVI SiC matrix [11][10][12]. They identified lower shear strength in push-out tests on composites made with HN-S fibres compared to SA3 fibres and also an effect of pyrocarbon texture and thickness. Our values are within the range of measurements reported in the publications by Buet *et al.*, while also indicating that variation in manufacturing processes and microstructure impacts mechanical properties making precise comparison between different material suppliers challenging, even if nominally the same material has been manufactured.

Herbretau *et al.* suggest an approach using a modified equation for debond strength based on accounting for crack initiation at the top surface of the sample and propagation along the interface, rather than simply averaging the force across the entire surface area [13]. Using this method, they calculated 160-220 MPa as the critical debond stress from a Nicalon fibre composite with PyC interphase and CVI SiC matrix with additional boron carbide and silicon carbide layers to make a composite different to our work [13]. Their value includes the effect of friction and geometry due to swelling during the interface failure. Without their analytical adjustment, the debond strength in their three tests based on simple surface area calculation and their reported dimensions is 115-159 MPa, i.e. the adjustment increases shear strength by approximately 39% for their experiments. Mueller *et al.* also provide a different analytical adjustment to account for the stable and unstable interfacial crack propagation length in another variant of SiC/PyC/SiC composite [33]. While these values are in the same order of magnitude as ours and other published values from Buet *et al.* and Hussey *et al.* the different material grades means the measured mechanical properties will be different. Earlier work on older types of SiC fibres by Yang and Hinoki showed higher debond strength ~300MPa for ~100nm PyC coatings, although their experiments used sharp indenters rather than flat punch indenter tips [34][35].

Micro fibre push-out testing appears to be an appropriate method to directly measure interfacial debond stress without analytical adjustments as debonding is instantaneous across the entire interface with a known and well-defined gauge length. As this property is a vital input for multi-scale performance models of composites, we consider that it should be measured directly rather than indirectly [36]. This can be achieved using micro fibre push-out testing but not using long fibre push-out testing. Weibull analysis can be used to account for different interfacial surface areas in different gauge length tests, for example, when different ion irradiation conditions are used with different damage range, as long as the fibre remains "short".

An alternative approach to characterize the fibre-matrix interface is the micropillar sliding method. Shih, Kabel, and Karakoc et al. have all measured debond stresses in SiC_f/SiC composites with PyC interphase using this method for various composites with Hi-Nicalon Type-S (HNS) or Tyranno SA3 fibres and CVI SiC matrices [37, 38, 39]. Depending on the grade, debond stresses were calculated between 36 MPa and 266 MPa. HNS fibres have a smoother surface than SA3 (and SA4) fibres; for SA3 fibres similar to those used in this work, debond stresses of 95 MPa, 152 MPa, and 145 MPa were determined for varying grades [38, 39]. The micropillar method significantly alters the mechanical testing situation as the test is not axially symmetric, and it removes any residual stress effects, or effects of fibre shape such as the taper effect which has been shown to be important. The dominant correlation of interfacial strength with a micromechanical testing size effect has been found with interfacial surface area, where an area greater than 160 μm^2 has been approximated as representative of a long fibre push-out test. These micropillar sliding tests are conducted with a significantly smaller interfacial surface area of only a few microns square, vastly reducing the likelihood of statistical defects and resulting in a higher debond stress which is more akin to the micro fibre push-out tests in this work. The benefit of this method is that fibre geometry such as taper is removed allowing easier evaluation of the interfacial sliding friction coefficient.

4.2. Fibre push-out mechanisms, microstructural effects, and implications

Elucidated by the finite element modelling and experimental characterisation, the micro fibre push-out mechanism consists of four steps:

1. Elastic loading of the fibre.
2. Crack initiation on the bottom face of the fibre at peak stress (see Appendix F).
3. Crack propagation along the interface.
4. Frictional sliding as the fibre is pushed out.

Various parameters affect the characteristics of each of these steps in the push-out mechanism. Experimentally, step 1 is preceded by a small bedding in a period as the flat

punch tip contacts the surface and any surface impurities or irregularities are compressed. SEM images of the indenter tip used in these experiments show debris adhered to the surface, shown in Figure E.26(a) of the supplementary material, and that the tip istelf is not perfectly flat.

FEM simulations predict that fracture initiates from the bottom of the fibre in the micro push-out tests (See Figure F.27). This is caused by the bottom face of the "bridge" being put into tension by slight bending, also reducing the friction in that area. Although this happens, changes to Mode I properties do not affect the load displacement data, two explanations are possible to justify this: The first one is that the failure is almost instantaneous, indicating that regardless of the crack initiation being on the top or bottom surface, the test is Mode II shear debonding. This is in agreement with De Meyere et al. who performed trench fibre push-outs on the edge of a SiC_f/BN/SiC composite to observe the deformation behaviour during push-out tests [14]. The second one is the reduced friction in the bottom faces which causes a reduced Mode II resistance compared with the rest of the interface.

A key consideration for fibre push-out testing is that it presents more friction than the fibre pull-out mechanism that occurs during the macroscopic failure of a composite. The reason is the Poisson expansion of fibres during the push-out compression causes an increased normal force and higher friction that increases the interface toughness. The debonding initiation on the bottom of the "bridge" in micro push-out tests may be more representative of the actual fibre pull-out behaviour in a macroscopic since the friction is reduced due to "bridge" bending compared to a long fibre push-out test.

Steps 2, 3, and 4 could not be differentiated in the long fibre push-out tests as the G200 instrument is load controlled and there is a displacement jump once the fibre is detached. The in-situ tests conducted in displacement control show a load drop with a second lower peak immediately after initial debonding and frictional sliding. This characteristic double peak could not be replicated in the FEM simulations. The second load peak could be caused by a larger asperity on the fibre surface roughness impinging on an asperity on the matrix surface, similar to what can be seen in the cross-sections in Figure 6 (c) and (f). This would need a continued force to overcome after some further displacement has occurred after initial debonding. Another explanation may be the spalling of interphase PyC causing a local barrier to be overcome. This may explain the scratches on the interphase which is seen for all tests regardless of the gradient of the frictional component in step 4. In short fibre tests, crack initiation and propagation appear to be almost instantaneous, i.e. the whole interface debonds at once.

Step 4 frictional sliding requires a clamping stress determined by the Coulomb friction coefficient and a surface normal force. This is simple to evaluate if a perfectly parallel fibre is assumed, however, in these short fibre tests, even small tapers in the fibre dominate frictional sliding forces to the extent that the gradient is positive even as the contact length is reduced during push-out. This makes evaluating a friction force experimentally challenging using this method, at least on the SA4 fibre reinforced composite in this work.

Raman spectroscopy has been used to measure residual stress in the matrix and fibre of a micro push-out test. Before the test, SiC in the fibre is approximately stress-free based on the position of the TO peak. The large compressive stress observed from the D and G band signals for carbon pockets in the SiC fibre is likely from manufacturing processes as the carbon pockets are completely surrounded by SiC grains within the fibre. Characterising the structure and properties of these carbon pockets is beyond the scope of this paper. SiC in the matrix around the fibre is in tension as determined by the TO peak being 2 cm^{-1} lower than the stress-free position of 6H-SiC if we base the dominant signal as arising from stacking faults in 3C-SiC rather than considering the weak 3C-SiC TO Raman signal. Assuming a plane stress state based on the shallow 1 µm penetration depth of the Raman probe laser, the tensile stress is 850 MPa in the CVI SiC matrix [40, 41]. Following push-out, the SiC TO peak of the fibre is at 799 cm^{-1}, 3 cm^{-1} higher wavenumber than the fibre before push-out testing and the literature stress-free peak position of 3C-SiC. This indicates a compressive residual stress of -1.27 GPa after push-out testing based on a plane stress approximation for the laser interaction volume being at the free surface. This is consistent with the hypothesis of a positively tapered fibre pushing into the hole and being compressed as it is pushed deeper, which agrees with the positive gradient of the frictional component of the mechanical test data. A similar process can be followed for the carbon pockets in the fibres where the G band peak is at 1594 cm^{-1} before pushout and 1598 cm^{-1} after pushout. Taking 1594 cm^{-1} as the reference peak position for this structure of carbon, Δ_0, gives $\Delta\omega$ = +4 cm^{-1}. Carbon pockets will be in a hydrostatic stress state as they are small relative to the Raman probe volume and are completely surrounded by SiC rather than having a free surface. Based on the stress conversion method from [28]

a change in compressive stress of -1.28 GPa is calculated for carbon pockets in the SiC fibre after push-out testing, relative to their initial stress state. This is almost identical to the change in compressive stress on the SiC grains in the fibre calculated by Raman spectroscopy. After push-out, the matrix SiC peak position is at 788 cm^{-1}, i.e. 1 cm^{-1} higher than the pre-push-out case, but still in residual elastic tension by 1 cm^{-1} relative to the literature value for stress-free 6H-SiC. Since Raman measurements are made at the surface, the region of matrix SiC which is being measured is no longer constrained by the misfitting fibre at the centre, thus the as-manufactured residual tensile stress is partially relaxed in the matrix by the push-out test. This situation is similar to the case of a larger misfitting fibre in a hole, and could be introduced during CVD processing where the coating is deposited at high temperature over the fibre preform, then cooled to room temperature resulting in contraction and the measured tensile residual elastic stress. The coefficient of thermal expansion for SiC fibres is lower than for dense CVD SiC due to its lower density caused by residual carbon pockets, which results in the situation described above. The compliant PyC interphase is too thin to be directly measured, but could act as a buffer reducing the corresponding compressive stress on the fibre. This measurement confirms that there is a residual clamping stress on the fibre controlling the frictional sliding portion of these tests and the fibre pull-out toughening mechanisms. While absolute quantification of the stress state is challenging, approximations have been made here. Residual stress or clamping stress is a key engineering parameter which could potentially be optimised by manufacturing and microstructural design.

The shear lag theory [16, 26] traditionally models the friction at composite interfaces due to surface roughness, and has been extended to predict fibre taper shape response. Understanding the wear caused by this roughness is crucial for composites subjected to mechanical fatigue [42] or thermomechanical fatigue loading [43], as found in applications like fusion blankets.

Significant research has contributed to the modelling of wear for multifibre composites. For instance, Longbiao [44] developed a wear model integrated with a statistical framework assuming a Weibull distribution of fibre strength. This approach was effectively applied to experiments involving SiC/SiC and SiC/C composites [45].

Rouby et al. [43] provide insights into the single-fibre interface by simplifying shear lag theory [26] using a first-order Taylor expansion of Equation 3.10. This formulation models friction wear in fibre push-out and push-back experiments [46]:

$$P_{\text{fric}} = \frac{C_{\text{Diff}}}{R(u)} 2\pi R(u)\mu\Lambda(t-u) \tag{4.3}$$

Where the radius is assumed nearly constant, $R(u) \approx R$. C_{Diff} encompasses geometric effects contributing to friction, influenced by roughness and thermal/mechanical swelling (these effects were negligible compared to positive taper shape in Equation 3.10, thus omitted in Subsection 3.7).

Examining the force-displacement characteristics after crack completion (see Figure 7(b)), most fibres exhibit quasi-linear force response with displacement, suggesting that $C_{\text{Diff}} \approx$ constant with minimal roughness wear.

The limited wear effect may be attributed to the relatively small tip displacement during the short-fiber push-out process (1-2 (μm)), in contrast with the roughness wavelength, which is approximately 0.5 (μm) as estimated from Figure 6(c, f). This wavelength represents the average distance between irregularity peaks, calculated using the Fourier transformation of the roughness profile [26]. However, we do not observe a significant difference in the proportionality between wavelength and displacement when compared to the experiments by Rouby et al. [43, 46], which reported a roughness wavelength of 5-10 (μm) and a tip displacement of 50-100 (μm).

Rouby et al. aimed to minimise fibre gauge length to mitigate the effects of fibre swelling during push-out, using fibres with a diameter of 0.1 mm and a gauge length of 0.6-3 mm [46]. While this approach is not as optimal as in short-fiber push-out (where fibers have diameters of 8-10 (μm) and gauge lengths of 1-10 (μm)), in which fracture occurs nearly instantaneously at the interface, we believe that the influence of swelling should not result in significant discrepancies.

The primary significant difference between the two push-out experiments lies in the dimensions of the sliding area at the interface. In the experiments conducted by Rouby et al., the sliding area dimensions were on the order of (mm^2), while the roughness wavelength and amplitude were on the order of (μm). Conversely, in the case of short fibres, both roughness and sliding area dimensions are on the order of (μm). The smaller sliding area results in lower statistical representation of the roughness profile, potentially neglecting significant irregularities associated with the taper effect in short fibres, which may be more susceptible to wear.

In conclusion, investigating the wear of roughness in

short fibres presents significant challenges due to the small size of the sliding area in relation to the roughness features. Additionally, experiments such as push-back tests, designed to assess friction fatigue or investigate effects like seating drop or velocity dependence, are further complicated by these size constraints. Conversely, while push-out experiments with long fibres are feasible, the greater length relative to the fibre area results in excessive swelling, which complicates comparisons with the findings from Rouby et al. Thus, a more intricate experimental setup is required for a comprehensive analysis of roughness wear in micro-sized fibres. The short fibres serve to isolate fracture properties which should be subsequently used in an analysis of longer fibres.

During irradiation, SiC composites undergo many changes which will impact their mechanical performance [1]. Significant degradation of the interphase at high doses is likely to change the debond stress and crack propagation [4, 5]. Dimensional changes in the fibre relative to the matrix will affect the residual stresses, the normal force on the fibre surface, and the frictional component of fibre pull-out mechanisms and push-out testing. At high doses, SiC fibres have been observed to shrink and densify while SiC matrices swell and expand causing a geometric mismatch across the interface [47]. The combination of fibre shrinkage and matrix swelling will relieve radial residual stress, reducing the surface normal force and the frictional component of SiC fibre composite mechanics. The swelling of high purity SiC by displacement damage has been extensively characterised and is well understood in fission reactor conditions, but is likely to be different due to higher transmutation rates in fusion reactor conditions [30, 48, 49]. Metallic transmutation products may form silicide or carbide precipitates [50, 51] and gaseous helium or hydrogen can form bubbles within a composite microstructure [52, 30, 53, 54]. The combined effects of displacement and transmutation damage in a fusion environment will likely be different to displacement damage and low transmutation rates in a fission neutron spectrum. Accelerated transmutation and displacement damage can only be studied by ion implantation, which requires advanced methods to characterise these thin layers. Accelerated testing enables us to understand these changes at a microstructural length scale, enabling us to predict the performance degradation of composites as a function of fusion reactor operating conditions, and allow us to design optimal microstructures and material grades to survive in these conditions. Measuring changes to interfacial debonding stress and frictional components after fusion-relevant ion irradiation is essential to understand the performance of SiC_f/SiC composites. Displacement-controlled micro push-out testing is potentially the most representative method of measuring these properties, and will be used to evaluate ion irradiated SiC_f/SiC composites in future work.

5. Conclusions

The technique of micro push-out testing has been demonstrated on nuclear grade SiC_f/SiC composites with gauge lengths within the obtainable range of ion implantation experiments. This technique provides new benefits over other micromechanical methods, such as micropillar sliding, as it retains most of the geometric constraints of fibres in a composite component. Additionally, compared to long fibre push-out experiments, it is easier to isolate properties such as debond stress from friction, and it is easier to model with faster and simpler simulations. Drawbacks include the relatively higher cost of FIB sample preparation, being constrained to testing fibres close to the edge of a specimen, defining a ”long” or a ”short” fibre, and higher sensitivity to local fibre geometry, which is averaged out in long fibre push-out experiments.

Various parameters have been studied using experiments and finite element modelling to ascertain their relative importance and impact on push-out mechanisms and material properties. Debond stress is minimally affected by residual stress, geometric taper in the fibre, or changes in interface properties such as toughness, roughness, or friction coefficient. Axial misorientation of the fibre has no detectable effect within the scatter of experimental measurements; force-displacement response is insensitive to misalignment, whether by sample preparation or fibre orientation differences within a unidirectional tow or woven fabric. However, axial misorientation has a detectable effect on debond stress in simulations for exaggerated angles beyond those obtained in experiments ($>10°$), being greater than the simple analytical adjustment for a tilted geometry. This suggests there is a change in the crack formation mechanism at large misorientation angles, which is not represented by Equation 3.9. Debond stress is therefore a robust value which can be extracted from micro push-out experiments and can be used for quantifying changes in fibre-interphase-matrix properties following shallow ion implantation damage, and which cannot be evaluated using long fibre push-out testing. Changes to other properties such as friction due to changes in fibre surface normal stresses can be measured by displacement controlled micro push-out testing.

The crack propagation and friction component of these experiments is affected noticeably by residual stress, interfacial friction (Coulomb) coefficient, and toughness as a property of the interphase. These determine the bulk toughness of the composite component at the crack deflection and fibre pull-out stage of mechanical failure. Different manufacturing methods, interphase deposition techniques or chemistries could be developed to beneficially tailor these properties which can be evaluated using various methods and tested before and after irradiation using the micro push-out technique.

Localised fibre taper has been found to be the dominant factor during the frictional component of micro push-out tests. In long fibre tests, local fibre tapers are averaged out along the length of the fibre; however, at these short gauge lengths, positive and negative tapers do not cancel out. This makes measuring a friction coefficient from these experiments challenging – a micropillar sliding test without geometric constraint is valuable here.

This micromechanical method allows prediction of the load-bearing ability of SiC composites beyond the proportional limit stress after irradiation, i.e. the strength of the fibre-matrix interface during crack bridging and before fibre pull-out mechanisms take effect. The method allows key fibre-matrix mechanical data to be measured and utilised as part of an experimentally informed multiscale mechanical performance model which can also be verified by micromechanical testing.

6. Acknowledgement

A. J. L. and E. T. were supported by the Royal Academy of Engineering under the Research Fellowship and Senior Research Fellowship programmes respectively. A. M. P. acknowledges the support from the framework of the EUROfusion Consortium, funded by the European Union via the Euratom Research and Training Program (Grant Agreement No. 12490 - EUROfusion) and from the EPSRC (grant number R76251/ CN001). The research used UKAEA's Materials Research Facility, which has been funded by and is part of the UK's National Nuclear User Facility and Henry Royce Institute for Advanced Materials. This work has been part funded by the EPSRC Energy Programme [grant number EP/W006839/1]. To obtain further information on the data and models underlying this paper, contact PublicationsManager@ukaea.uk. Views and opinions expressed are, however, those of the author(s) only and do not necessarily reflect those of the European Union or the European Commission. Neither the European Union nor the European Commission can be held responsible for these issues.

References

[1] Y. Katoh and L. L. Snead, "Silicon carbide and its composites for nuclear applications–historical overview," *Journal of Nuclear Materials*, vol. 526, p. 151849, 2019.

[2] B. Yang, X. Zhou, and Y. Chai, "Mechanical properties of sicf/sic composites with pyc and the bn interface," *Ceramics International*, vol. 41, no. 5, Part B, pp. 7185–7190, 2015.

[3] J. Delage, E. Saiz, and N. Al Nasiri, "Fracture behaviour of sic/sic ceramic matrix composite at room temperature," *Journal of the European Ceramic Society*, vol. 42, no. 7, pp. 3156–3167, 2022.

[4] T. Nozawa, T. Koyanagi, Y. Katoh, and H. Tanigawa, "High-dose, intermediate-temperature neutron irradiation effects on silicon carbide composites with varied fiber/matrix interfaces," *Journal of the European Ceramic Society*, vol. 39, no. 8, pp. 2634–2647, 2019.

[5] A. G. Perez-Bergquist, T. Nozawa, C. Shih, K. J. Leonard, L. L. Snead, and Y. Katoh, "High dose neutron irradiation of hi-nicalon type s silicon carbide composites, part 1: Microstructural evaluations," *Journal of Nuclear Materials*, vol. 462, pp. 443–449, 2015.

[6] R. M. De Meyere, L. Gale, S. Harris, I. M. Edmonds, T. J. Marrow, and D. E. Armstrong, "Optimizing the fiber push-out method to evaluate interfacial failure in sic/bn/sic ceramic matrix composites," *Journal of the American Ceramic Society*, vol. 104, no. 6, pp. 2741–2752, 2021.

[7] O. Gavalda-Diaz, R. Manno, A. Melro, G. Allegri, S. R. Hallett, L. Vandeperre, E. Saiz, and F. Giuliani, "Mode i and mode ii interfacial fracture energy of sic/bn/sic cmcs," *Acta Materialia*, vol. 215, p. 117125, 2021.

[8] E. Callaway, P. Christodoulou, and F. Zok, "Deformation, rupture and sliding of fiber coatings in ceramic composites," *Journal of the Mechanics and Physics of Solids*, vol. 132, p. 103673, 2019.

[9] A. Hussey, R. De Meyere, C. Deck, D. Armstrong, and Y. Zayachuk, "Statistically sound application of fiber push-out method for the study of locally non-uniform interfacial properties of sic-sic fiber composites," *Journal of the European Ceramic Society*, vol. 40, no. 4, pp. 1052–1056, 2020.

[10] E. Buet, C. Sauder, S. Poissonnet, P. Brender, R. Gadiou, and C. Vix-Guterl, "Influence of chemical and physical properties of the last generation of silicon carbide fibres on the mechanical behaviour of sic/sic composite," *Journal of the European Ceramic Society*, vol. 32, no. 3, pp. 547–557, 2012.

[11] E. Buet, C. Sauder, D. Sornin, S. Poissonnet, J.-N. Rouzaud, and C. Vix-Guterl, "Influence of surface fibre properties and textural organization of a pyrocarbon interphase on the interfacial shear stress of sic/sic minicomposites reinforced with hi-nicalon s and tyranno sa3 fibres," *Journal of the European Ceramic Society*, vol. 34, no. 2, pp. 179–188, 2014.

[12] E. Buet, J. Braun, and C. Sauder, "Influence of texture and thickness of pyrocarbon coatings as interphase on the mechanical behavior of specific 2.5d sic/sic composites reinforced with hi-nicalon s fibers," *Coatings*, vol. 12, no. 5, 2022.

[13] M. Herbreteau, S. Jouannigot, P. Weisbecker, A. Coradi, and E. Martin, "A new push-out procedure for the evaluation of interfacial properties of sic/sic composites," in *ECCM15-15TH European Conference On Composite Materials, Venice, Italy*, pp. 2–4, 2012.

[14] R. M. De Meyere, K. Song, L. Gale, S. Harris, I. M. Edmonds, T. J. Marrow, E. Saiz, F. Giuliani, D. E. Armstrong, and O. Gavaldà-Diaz, "A novel trench fibre push-out method to evaluate interfacial failure in long fibre composites," *Journal of Materials Research*, vol. 36, pp. 2305–2314, 2021.

[15] G. Lin, P. Geubelle, and N. Sottos, "Simulation of fiber debonding with friction in a model composite pushout test," *International journal of solids and structures*, vol. 38, no. 46-47, pp. 8547–8562, 2001.

[16] A. Martinez-Pechero, Y. Zayachuk, A. Widdowson, D. E. Armstrong, and E. Tarleton, "Obtaining sic fibers–pyc interfacial properties through push-out fem models," *Journal of the European Ceramic Society*, vol. 44, no. 2, pp. 784–794, 2024.

[17] P. H. Geubelle and J. S. Baylor, "Impact-induced delamination of composites: a 2d simulation," *Composites Part B: Engineering*, vol. 29, no. 5, pp. 589–602, 1998.

[18] R. Wang, J. Han, J. Mao, D. Hu, X. Liu, and X. Guo, "A molecular dynamics based cohesive zone model for interface failure under monotonic tension of 3d four direction SiCf/SiC composites," *Composite Structures*, vol. 274, p. 114397, 2021.

[19] G. Alfano and E. Sacco, "Combining interface damage and friction in a cohesive-zone model," *International Journal for Numerical Methods in Engineering*, vol. 68, no. 5, pp. 542–582, 2006.

[20] M. Smith, *ABAQUS/Standard User's Manual, Version 6.14*. United States: Dassault Systèmes Simulia Corp, 2022.

[21] J. Petrovic, "Weibull statistical fracture theory for the fracture of ceramics," *Metallurgical Transactions A*, vol. 18, pp. 1829–1834, 1987.

[22] Y. Zayachuk, P. Karamched, C. Deck, P. Hosemann, and D. E. Armstrong, "Linking microstructure and local mechanical properties in sic-sic fiber composite using micromechanical testing," *Acta Materialia*, vol. 168, pp. 178–189, 2019.

[23] K. Morishita, S. Ochiai, H. Okuda, T. Inshikawa, M. Sato, and T. Inoue, "Fracture toughness of a crystalline silicon carbide fiber (tyranno-sa3®)," *Journal of the American Ceramic Society*, vol. 89, no. 8, pp. 2571–2576, 2006.

[24] J. Kabel, P. Hosemann, Y. Zayachuk, D. E. Armstrong, T. Koyanagi, Y. Katoh, and C. Deck, "Ceramic composites: A review of toughening mechanisms and demonstration of micropillar compression for interface property extraction," *Journal of materials research*, vol. 33, no. 4, pp. 424–439, 2018.

[25] Z. C. Xia and J. W. Hutchinson, "Mode ii fracture toughness of a brittle adhesive layer," *International Journal of Solids and Structures*, vol. 31, no. 8, pp. 1133–1148, 1994.

[26] T. A. Parthasarathy, D. R. Barlage, P. D. Jero, and R. J. Kerans, "Effect of interfacial roughness parameters on the fiber pushout behavior of a model composite," *Journal of the American Ceramic Society*, vol. 77, no. 12, pp. 3232–3236, 1994.

[27] S.-i. Nakashima and H. Harima, "Raman investigation of sic polytypes," *physica status solidi (a)*, vol. 162, no. 1, pp. 39–64, 1997.

[28] O. Frank, G. Tsoukleri, I. Riaz, K. Papagelis, J. Parthenios, A. C. Ferrari, A. K. Geim, K. S. Novoselov, and C. Galiotis, "From graphene to carbon fibres: Mechanical deformation and development of a universal stress sensor," *arXiv preprint arXiv:1010.1072*, 2010.

[29] A. J. Leide, R. I. Todd, and D. E. Armstrong, "Measurement of swelling-induced residual stress in ion implanted sic, and its effect on micromechanical properties," *Acta Materialia*, vol. 196, pp. 78–87, 2020.

[30] M. Rigby-Bell, A. Leide, V. Kuksenko, C. Smith, G. Zilahi, L. Gale, T. Razzell, J. Wade-Zhu, and D. Bowden, "The response of silicon carbide composites to he ion implantation and ramifications for use as a fusion reactor structural material," *Journal of the European Ceramic Society*, vol. 43, no. 16, pp. 7390–7402, 2023.

[31] W. F. Skerjanc and B. P. Collin, "Assessment of material properties for triso fuel particles in parfume," tech. rep., Idaho National Lab.(INL), Idaho Falls, ID (United States), 2018.

[32] A. Doitrand, R. Henry, T. Lube, and S. Meille, "Size effect assessment by Weibull's approach and the coupled criterion," *Engineering Fracture Mechanics*, vol. 256, p. 107979, oct 2021.

[33] W. Mueller, J. Moosburger-Will, M. Sause, M. Greisel, and S. Horn, "Quantification of crack area in ceramic matrix composites at single-fiber push-out testing and influence of pyrocarbon fiber coating thickness on interfacial fracture toughness," *Journal of the European Ceramic Society*, vol. 35, no. 11, pp. 2981–2989, 2015.

[34] W. Yang, A. Kohyama, T. Noda, Y. Katoh, T. Hinoki, H. Araki, and J. Yu, "Interfacial characterization of cvi-sic/sic composites," *Journal of Nuclear Materials*, vol. 307-311, pp. 1088–1092, 2002.

[35] T. Hinoki, W. Zhang, A. Kohyama, S. Sato, and T. Noda, "Effect of fiber coating on interfacial shear strength of sic/sic by nano-indentation technique," *Journal of Nuclear Materials*, vol. 258-263, pp. 1567–1571, 1998.

[36] Y. Chen and J. Marrow, "Effect of irradiation swelling on the mechanical properties of unidirectional sic/sic composites: A numerical investigation at microstructural level," *Journal of Nuclear Materials*, vol. 569, p. 153918, 2022.

[37] C. Shih, Y. Katoh, K. J. Leonard, H. Bei, and E. Lara-Curzio, "Determination of interfacial mechanical properties of ceramic composites by the compression of micro-pillar test specimens," *Journal of Materials Science*, vol. 48, pp. 5219–5224, 2013.

[38] J. Kabel, Y. Yang, M. Balooch, C. Howard, T. Koyanagi, K. A. Terrani, Y. Katoh, and P. Hosemann, "Micro-mechanical evaluation of sic-sic composite interphase properties and debond mechanisms," *Composites Part B: Engineering*, vol. 131, pp. 173–183, 2017.

[39] O. Karakoc, T. Koyanagi, T. Nozawa, and Y. Katoh, "Fiber/matrix debonding evaluation of sicf/sic composites using micropillar compression technique," *Composites Part B: Engineering*, vol. 224, p. 109189, 2021.

[40] A. J. Leide, R. I. Todd, and D. E. Armstrong, "Effect of ion irradiation on nanoindentation fracture and deformation in silicon carbide," *Jom*, vol. 73, no. 6, pp. 1617–1628, 2021.

[41] J. F. DiGregorio and T. E. Furtak, "Analysis of residual stress in 6h-sic particles within al2o3/sic composites through raman spectroscopy," *Journal of the American Ceramic Society*, vol. 75, no. 7, pp. 1854–1857, 1992.

[42] A. Pasto, D. Braski, T. Watkins, W. Porter, E. Lara-Curzio, and S. McSpadden, "Characterization techniques for composites and other advanced materials," *Composites Part B: Engineering*, vol. 30, no. 7, pp. 631–646, 1999.

[43] D. Rouby and N. Louet, "The frictional interface: a tribological approach of thermal misfit, surface roughness and sliding velocity effects," *Composites Part A: Applied Science and Manufacturing*, vol. 33, no. 10, pp. 1453–1459, 2002.

[44] L. Longbiao, "Modeling the effect of interface wear on fatigue hysteresis behavior of carbon fiber-reinforced ceramic-matrix composites," *Applied Composite Materials*, vol. 22, pp. 887–920, 2015.

[45] L. Longbiao, "Assessment of the interfacial properties from fa-

tigue hysteresis loss energy in ceramic-matrix composites with different fiber preforms at room and elevated temperatures," *Materials Science and Engineering: A*, vol. 613, pp. 17–36, 2014.

[46] H. Cherouali, G. Fantozzi, P. Reynaud, and D. Rouby, "Analysis of interfacial sliding in brittle-matrix composites during push-out and push-back tests," *Materials Science and Engineering: A*, vol. 250, no. 2, pp. 169–177, 1998.

[47] S. Kondo, T. Hinoki, M. Nonaka, and K. Ozawa, "Irradiation-induced shrinkage of highly crystalline sic fibers," *Acta Materialia*, vol. 83, pp. 1–9, 2015.

[48] L. L. Snead, T. Nozawa, Y. Katoh, T.-S. Byun, S. Kondo, and D. A. Petti, "Handbook of sic properties for fuel performance modeling," *Journal of nuclear materials*, vol. 371, no. 1-3, pp. 329–377, 2007.

[49] M. Sawan, Y. Katoh, and L. L. Snead, "Transmutation of silicon carbide in fusion nuclear environment," *Journal of Nuclear Materials*, vol. 442, no. 1-3, pp. S370–S375, 2013.

[50] W. Jiang, H. J. Jung, L. Kovarik, Z. Wang, T. J. Roosendaal, Z. Zhu, D. J. Edwards, S. Hu, C. H. Henager, R. J. Kurtz, and Y. Wang, "Magnesium behavior and structural defects in Mg+ ion implanted silicon carbide," *Journal of Nuclear Materials*, vol. 458, pp. 146–155, 2015.

[51] W. Jiang, S. R. Spurgeon, J. Liu, D. K. Schreiber, H. J. Jung, A. Devaraj, D. J. Edwards, C. H. Henager, R. J. Kurtz, and Y. Wang, "Precipitates and voids in cubic silicon carbide implanted with 25Mg+ ions," *Journal of Nuclear Materials*, vol. 498, pp. 321–331, 2018.

[52] B. T. Clay, S. E. Donnelly, and G. Greaves, "Observations of He platelets during He ion irradiation in 3C SiC," *Journal of Nuclear Materials*, vol. 559, feb 2022.

[53] X. Hu, T. Koyanagi, J. Zhao, T. Yamamoto, and Y. Katoh, "Microstructural evolution of 3C-SiC exposed to simultaneous neutron irradiation and helium implantation," *Journal of Nuclear Materials*, vol. 509, pp. 366–376, 2018.

[54] T. S. Duh, K. M. Yin, J. Y. Yan, P. C. Fang, C. W. Chen, J. J. Kai, F. R. Chen, Y. Katoh, and A. Kohyama, "Study of helium bubble formation in SiCf/PyC/β-SiC composites by dual-beam irradiation," *Journal of Nuclear Materials*, vol. 329-333, no. 1-3 PART A, pp. 518–523, 2004.

[55] A. Turon, C. G. Davila, P. P. Camanho, and J. Costa, "An engineering solution for mesh size effects in the simulation of delamination using cohesive zone models," *Engineering fracture mechanics*, vol. 74, no. 10, pp. 1665–1682, 2007.

[56] C. Liang and J. Hutchinson, "Mechanics of the fiber pushout test," *Mechanics of materials*, vol. 14, no. 3, pp. 207–221, 1993.

Appendix A. Raman spectroscopy analysis procedure

The Raman spectroscopy analysis workflow consisted of:

1. Cosmic ray removal, spectral smoothing, and background subtraction using a rolling shape function.
2. Principal component analysis to segment fibres and matrix.
3. Curve fitting using a combination of Gauss and Lorentz functions for the Si-C and C-C peaks.

Movements to lower relative Raman shifts indicate tensile stress, while higher relative Raman shifts indicate compressive stress for SiC and carbon peak positions [41, 28]. The carbon G band is most commonly used for residual stress calculations in carbon materials and a universal conversion factor for change in Raman shift has been proposed by Frank et al. where $\sigma = \frac{\omega_0}{5} \cdot \Delta\omega$ with stress in MPa, where ω_0 is the stress-free peak position which is assumed to be 1580 cm^{-1} however this is dependent on the exact phase of the graphite [28]. For SiC, stress conversion factors have been calculated by DiGregorio and Furtak with $\sigma = \Delta\omega \cdot -283$ where stress is in MPa [41]. These equations are assumed to be valid for hydrostatic stress states and can be adjusted for plane stress state by multiplying by 3/2 if the microstructure producing the signal is near the surface.

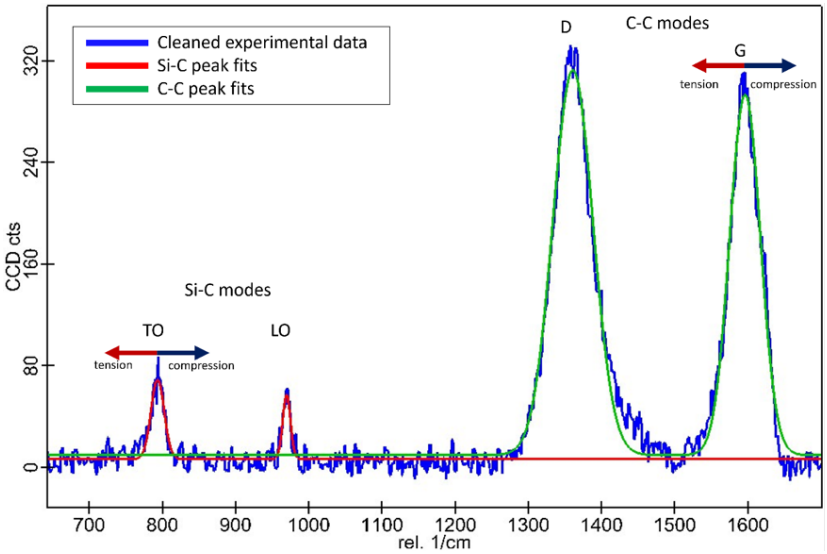

Figure A.21: Example of peak fitting functions for a SiC fibre spectrum.

Appendix B. Axial misorientation geometry

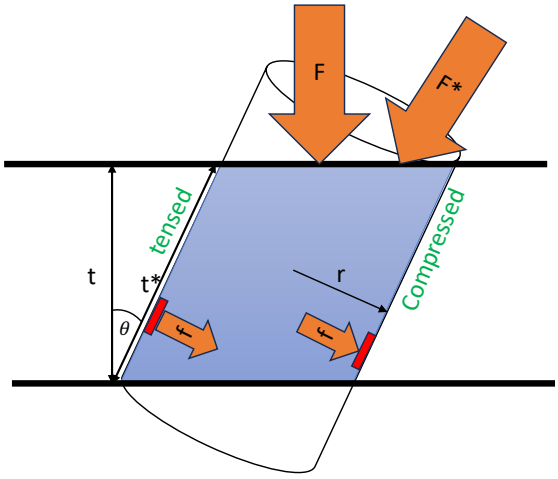

Figure B.22: Schematic of axial misorientation geometry.

Figure B.23 shows the complete debonding of a fibre misoriented by 20° through the cohesive damage D. This magnitude is 0 when the area is unaffected by damage and 1 when it is completely debonded (see Equation (2.3)). While the damage initiates in the compressed side (Figure B.23 3) and 4), indicated by the red arrow), the friction slows down the sliding (mode II crack) compared with the tensile side (Figure B.23 5)). The crack initiated at the tensile side propagates to the compressed side (Figure B.23 6) and 7)), but the friction slows down the process compared to a 0° short-fibre.

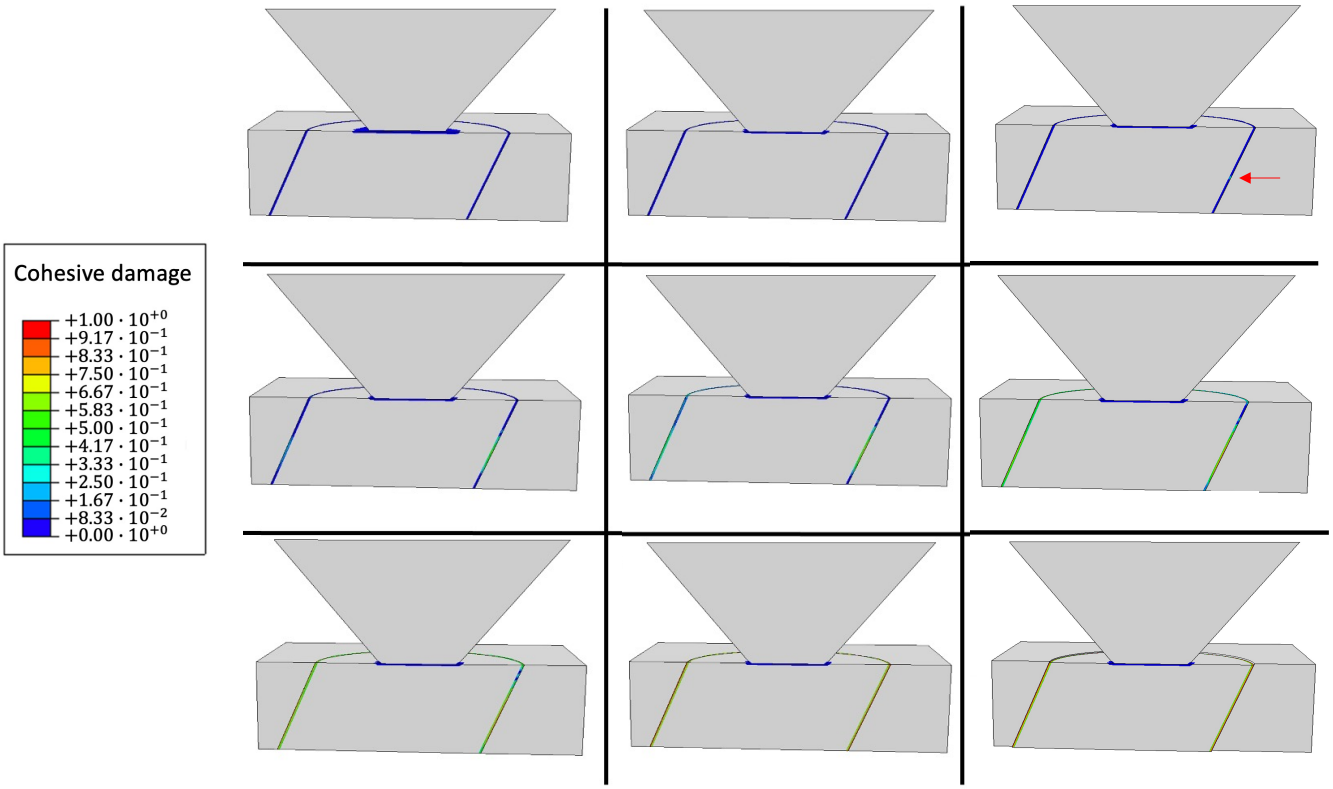

Figure B.23: Failure process of a fibre with an axial misorientation of 20°. The variable showed is the cohesive damage D defined in Equation (2.3). The red arrow indicates the point where the crack has been initiated.

Appendix C. FIB slice and view

The FIB milling artefact shown in Figure 5 is due to uneven platinum deposition and results in an approximately cylindrical milling artefact once the images are reconstructed. Once the Pt cap is segmented, this could look like an impression or some damage to the fibre from the indenter tip. However, Figure C.24 shows unsegmented images and the uneven deposition of platinum into the push-out impression and how this leads to the curtaining artefact during milling. Attempts to remove this using image processing during reconstruction e.g. ring removal algorithms, caused degradation of the image quality and contrast from the PyC layer which is also a ring in this dataset.

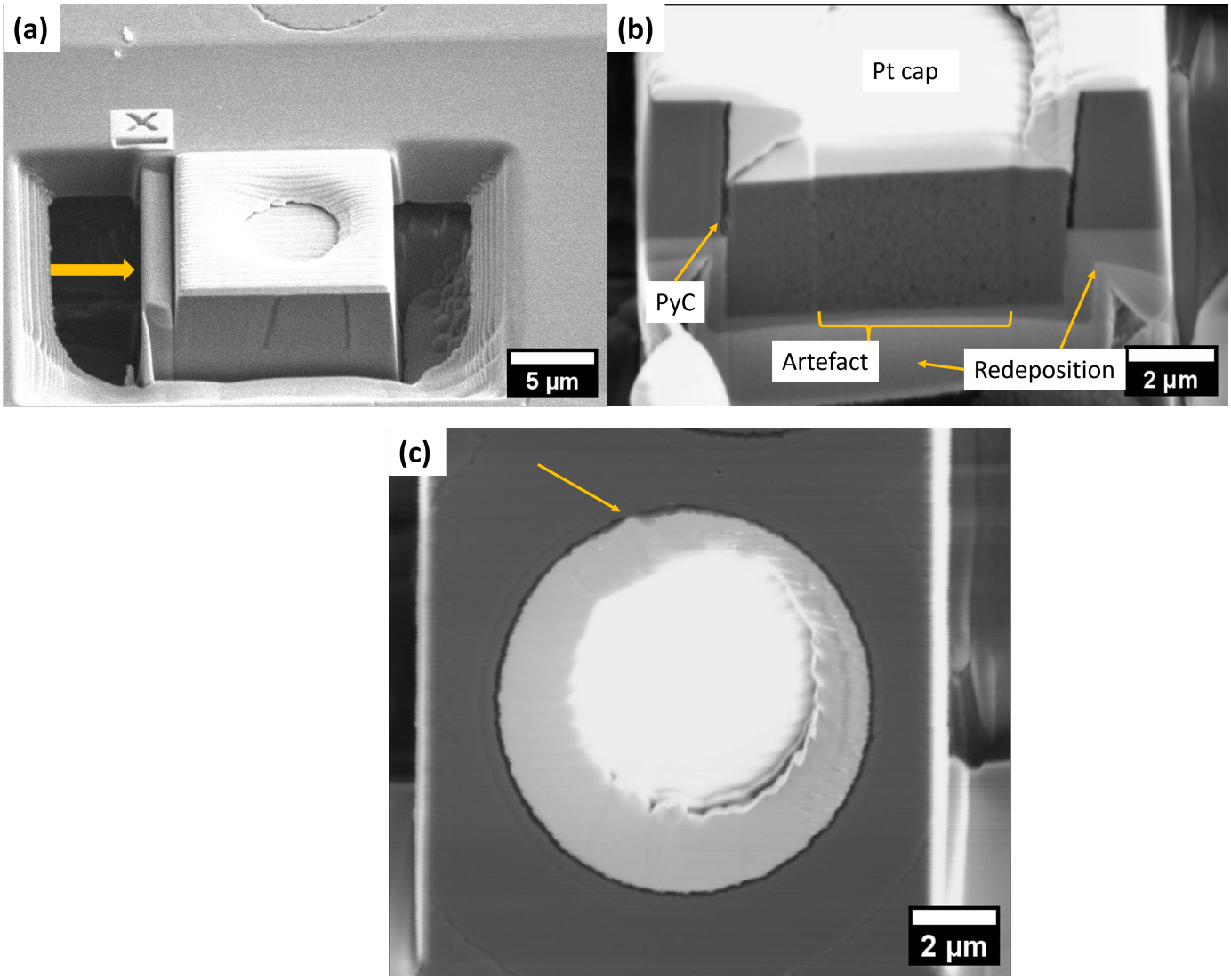

Figure C.24: Unsegmented SEM images of the slice and view procedure. (a) SEM image of the chunk before slicing and viewing. The yellow arrow indicates the direction of the undercut trench with the edge of the specimen on the left. (b) SEM image suring slice and view, not reconstructed. (c) Reconstructed horizontal slice within the Pt cap showing the uneven deposition. The yellow arrow shows where Pt has filled a gap or scratch in the PyC.

Appendix D. Fibre surface images

The surface of Tyranno SA4 fibres is rough with no features or texture parallel to the fibre length which could correspond to the scratches observed in PyC after push-out tests. The image below shows a fracture surface with exposed fibres revealing this roughness and no grooves or texture which could correspond to the impressions seen in the PyC. An impression from a dropped-out fibre also shows a random rough surface without texture.

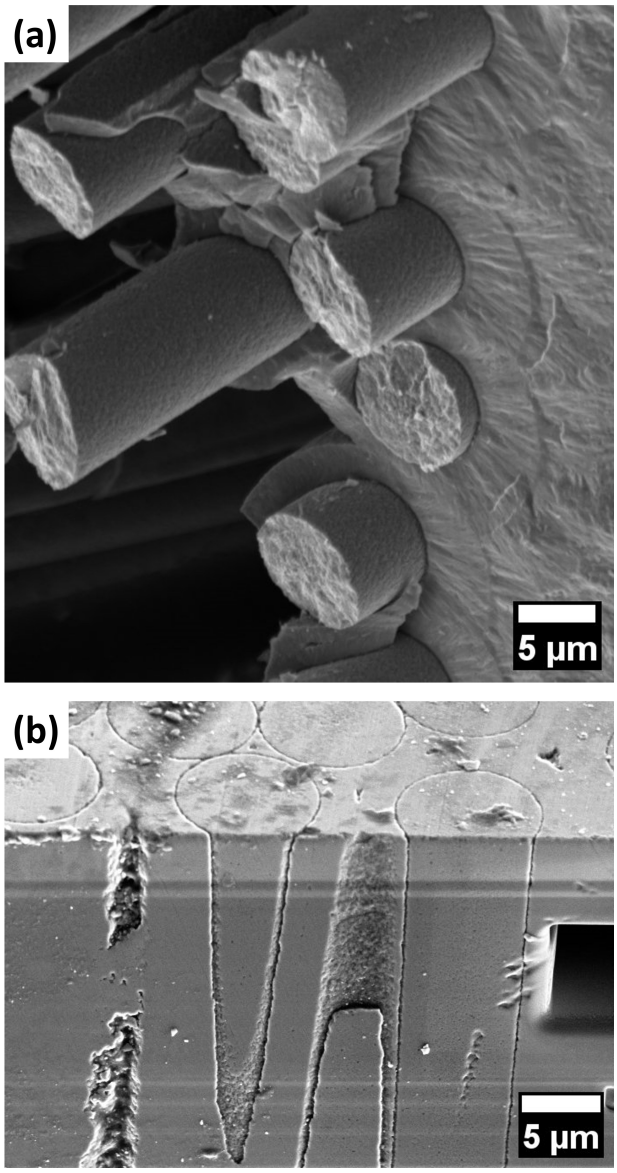

Figure D.25: (a) Fracture surface showing pulled out fibres with the randomly oriented rough surface. (b) Residual impression from where a fibre has partially dropped out during sample preparation, also showing a randomly oriented rough surface.

Appendix E. Experimental indenter tip effects

Figure E.26(a) shows an SEM image of the flat punch tip used for push-out testing. The nominally 5 µm diameter flat tip has a rounded square shape in reality and appears to be slightly concave rather than flat. Surface contamination or debris can be seen on the tip. Considering the extremely low loads for the testing here, the tip shape is unlikely to have a significant effect, and no evidence of plastic deformation or indentation was observed in the surfaces of pushed-out fibres. Parametric FEA studies of the effect of misorientation of the tip face (Figure E.26(b)) relative to the fibre surface found a minimal effect for these low loads.

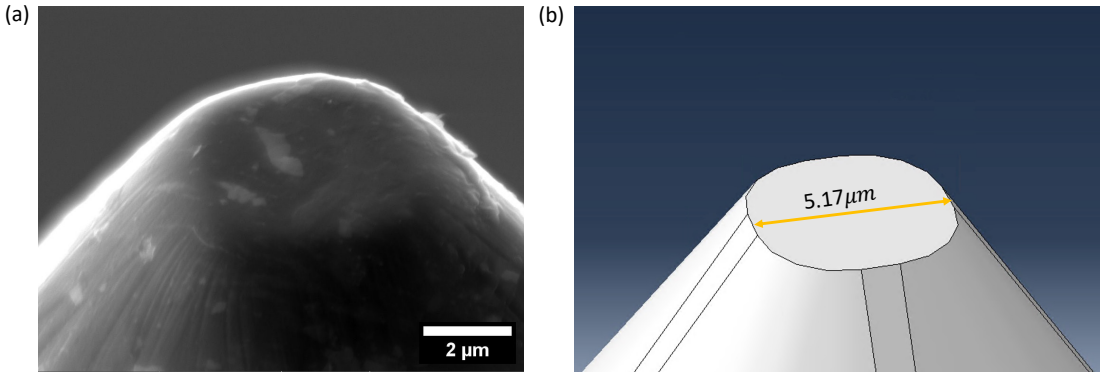

Figure E.26: (a) SEM image of flat punch tip used for in-situ pushout testing. (b) Flat tip reproduction in the FEA model.

Appendix F. Failure process of a short fibre

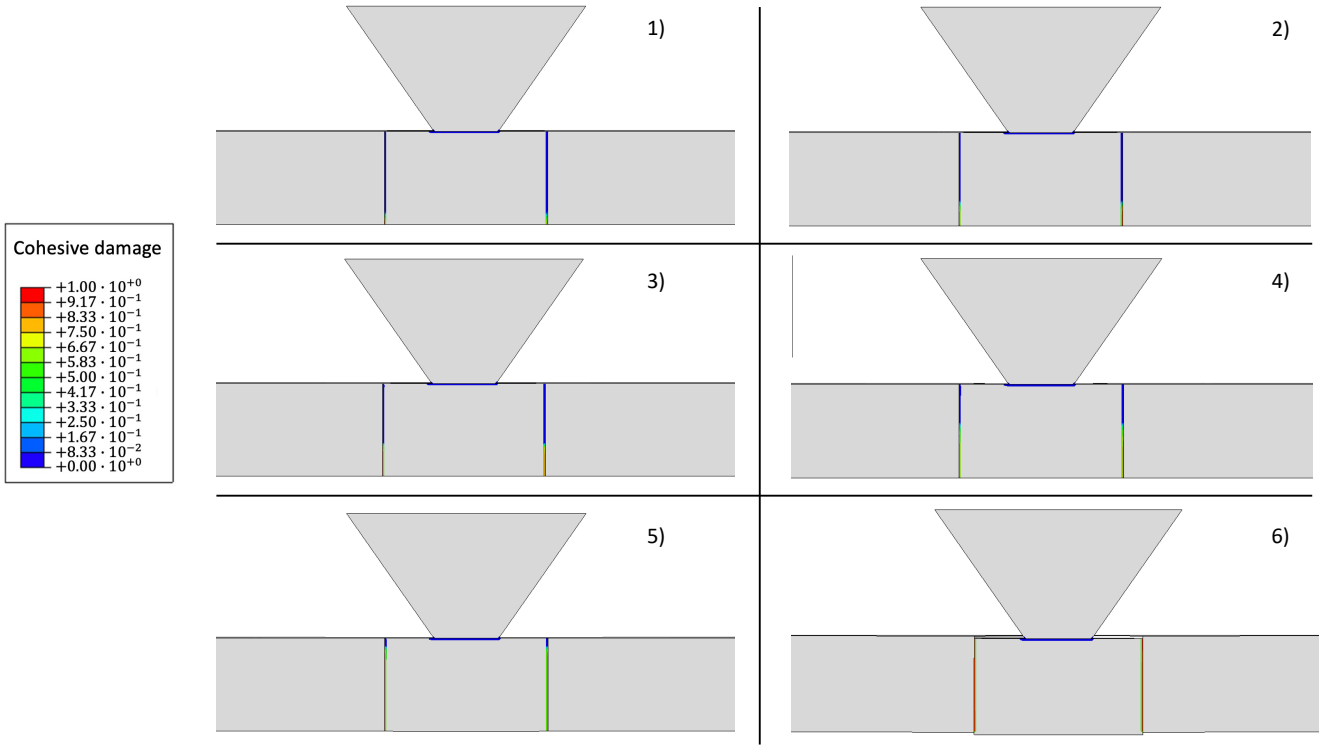

Figure F.27: Failure process of a short fibre. The variable D is the cohesive damage defined in Equation (2.3). The crack propagates from the bottom to the top face as it was observed experimentally in [14].

Appendix G. Mesh of the fibre-push out model.

In Figure G.28(a), the mesh seed applied to the fibre F6 is shown. Figure G.28(b) illustrates the matrix, Figure G.28(c) shows the fiber, and Figure G.28(d) depicts the indenter. A minimum mesh seed size of 0.2 μm is used in the region connecting the matrix and the fiber, where the interface consists of cohesive elements also measuring 0.2 μm. According to Turon et al. [55], the mesh size must be sufficiently small to ensure that the cohesive length, l_{cz}, is captured by 3-5 elements. The cohesive length is the characteristic distance ahead of a crack tip over which fracture processes occur in a material. This zone represents the area where cohesive forces act to resist the separation of crack surfaces. In [55], several definitions from the literature describe the cohesive length in the following form:

$$l_{cz} = ME^* \frac{G_c}{(\sigma^{\max})^2} \quad \text{where } \frac{1}{E_*} = \frac{1}{2}\left(\frac{1}{E_{PyC}} + \frac{1}{E_{Fibre}}\right) \tag{G.1}$$

Where $G_c = 10.5$ J/m^2 is the mode II toughness of the interface, $\sigma^{\max} = 86.9, 116and158$ MPa are the debond stresses for F6, B4 and B2 fibres respectively, E^*= 37 GPa is an estimation of the elastic modulus of the interface [56] defined by the elastic modulus of the PyC interface 20 GPa and the fibre 365 GPa [16] and M depends on the literature but generally is a value from 0.21 to 1 (it was used the smallest value to be conservatives). The minimum value would be $l_{cz} = 11.07, 6.06$ and 3.2 μm which results in a seed= 2.21, 1.21 and 0.65 μm for F6, B4 and B2 fibres respectively. These seeds are bigger than the interface seed; however, we decide to be conservative because the crack at the bottom of the fibre is a mix of mode II and I ($G_c = 2.5$ J/m^2 for mode I), requiring a smaller seed of 0.2 μm. The seeds create simulations of 235862, 325915 and 212003 elements for F6, B4 and B2 fibres, respectively.

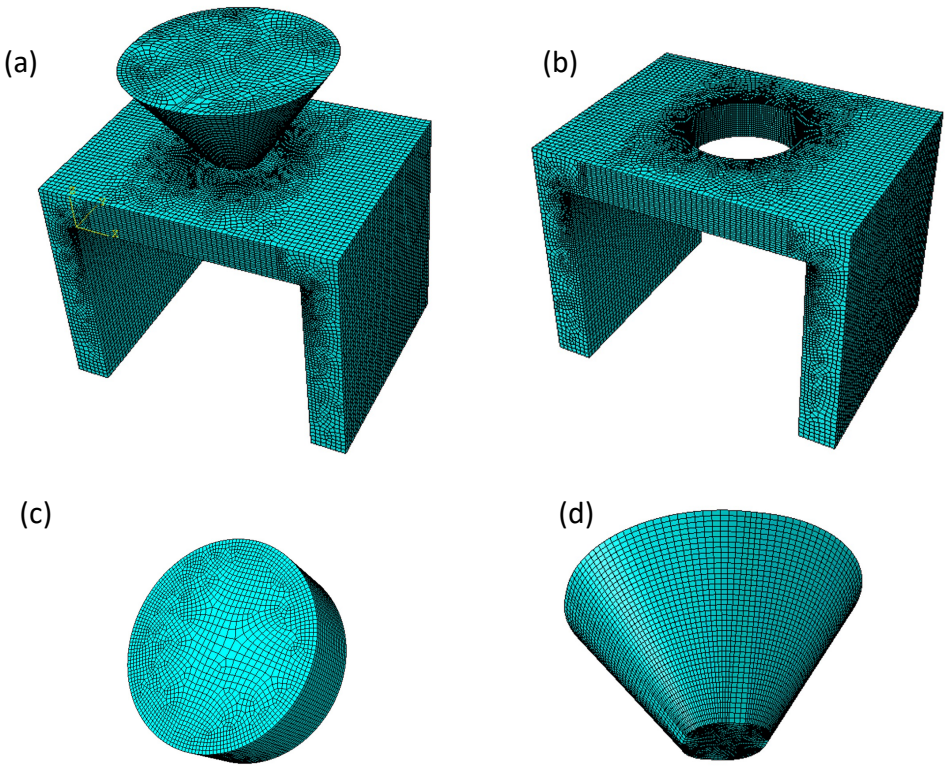

Figure G.28: Mesh of the different components of fibre push-out simulation F6.

Appendix H. Shear stress over the interface of Fibre F6

In short fibres, the distribution of shear stress exhibits a more uniform behaviour compared to that in long fibres. Utilising the software Abaqus, it is possible to visualise shear stress along the interface of fibre F6 as an example (represented by cohesive contact). The provided image represents the condition at the onset of damage, which occurs very close to the point of damage completion due to the rapid progression of this process.

The variation in colour observed within the stress profile arises from the positioning of the x=0 plane in the middle of the fibre, this causes the change of direction of X-coordinate and therefore it changes the sign of shear stress.

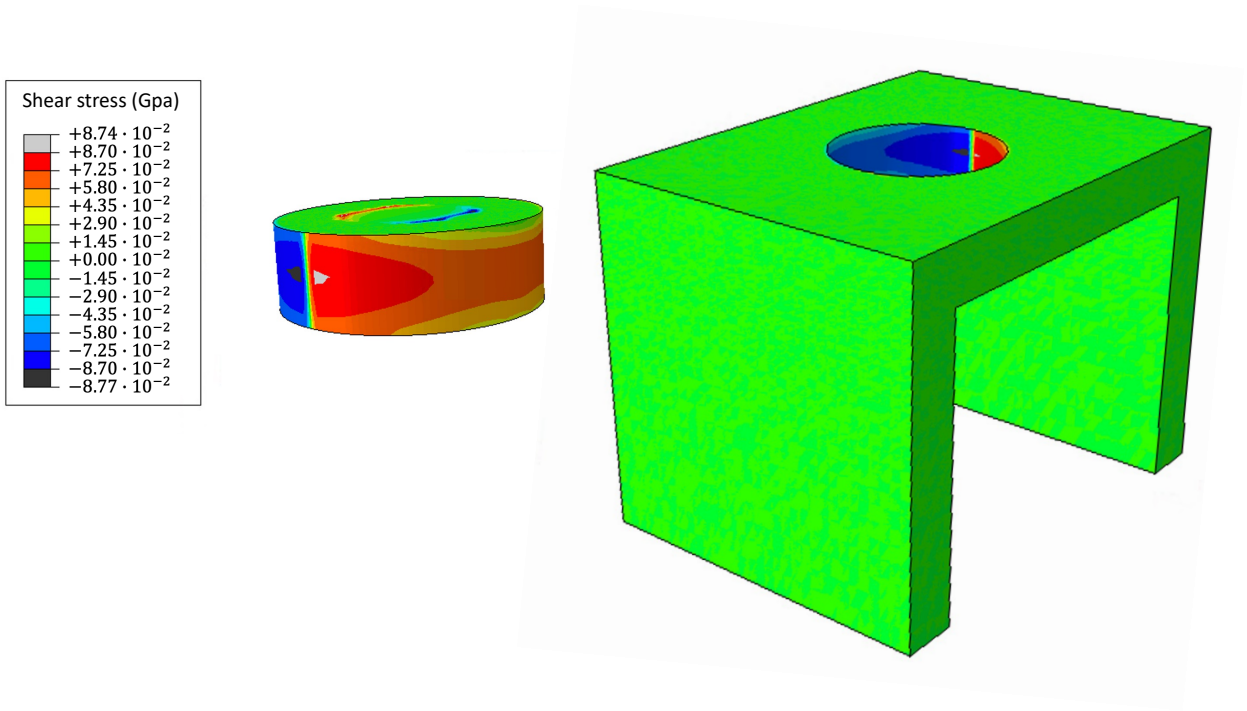

Figure H.29: Shear stress over the interface of fibre F6.

As illustrated, the shear stress distribution exhibits a high degree of uniformity, with more than 75% of the contact area reaching values close to the debond stress threshold of 87 MPa prior to crack initiation. It is important to note that the distribution is not perfectly homogeneous, primarily due to the geometric configuration of the fibre's experimental bridge shape. This introduces minor inhomogeneities in the stress field; however, these variations are negligible when compared to the stress profiles typically observed in long fibre specimens [16].

Appendix I. Von Mises stress distributions of adjusted push-out models

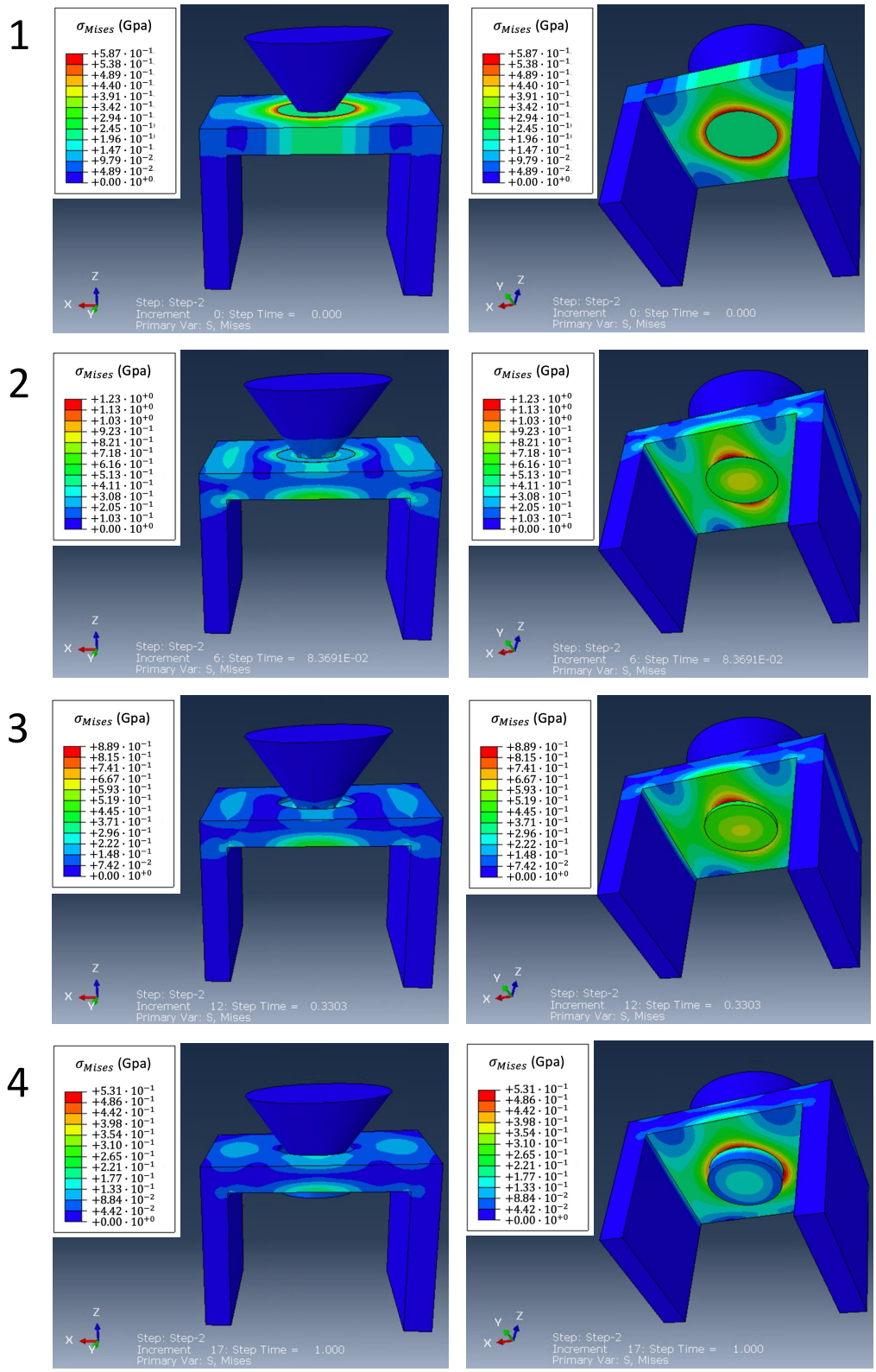

Figure I.30: Von Mises Stress profile of F6 from up and down perspectives for the different stages of indentation.

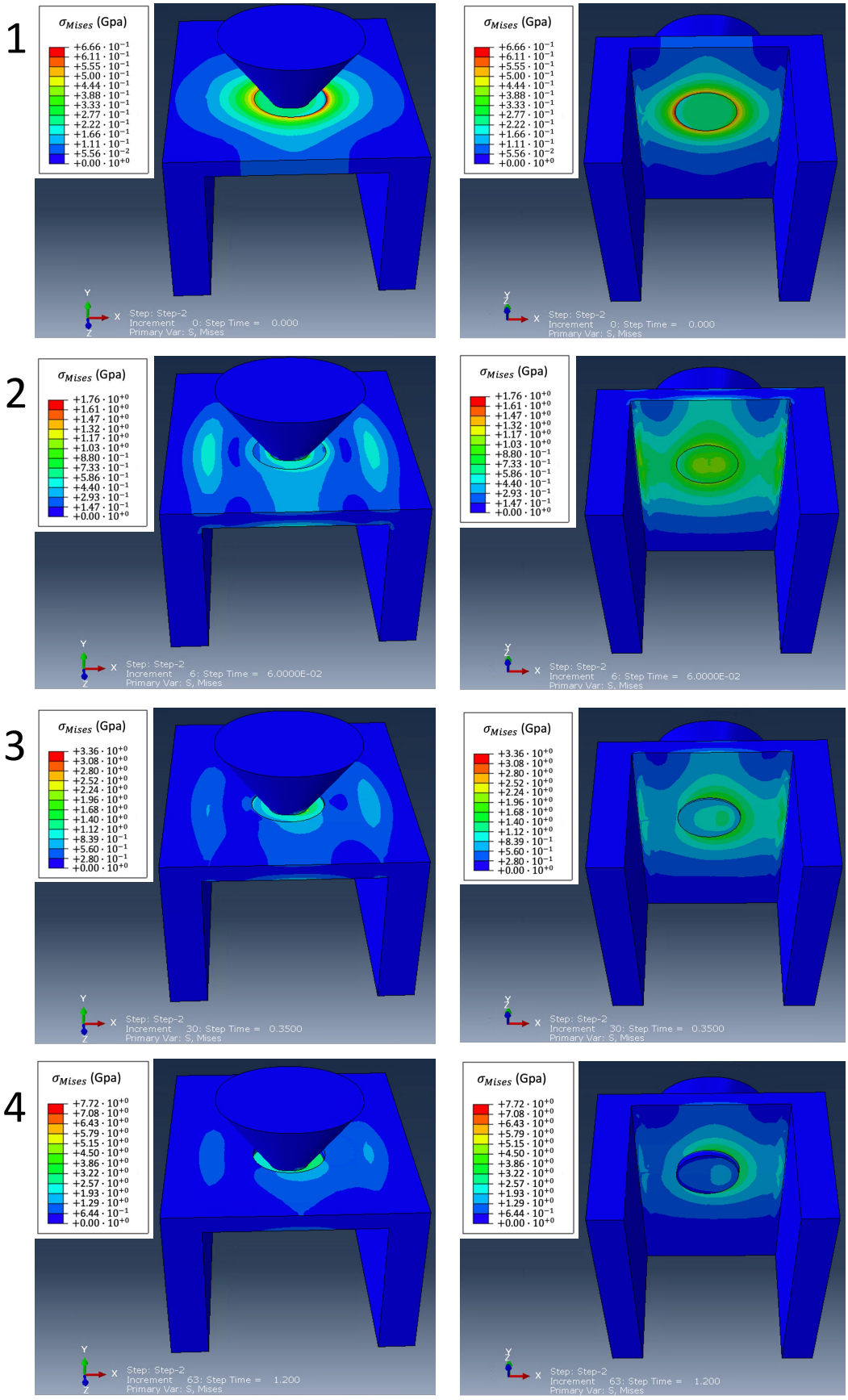

Figure I.31: Von Mises Stress profile of B2 from up and down perspectives for the different stages of indentation.

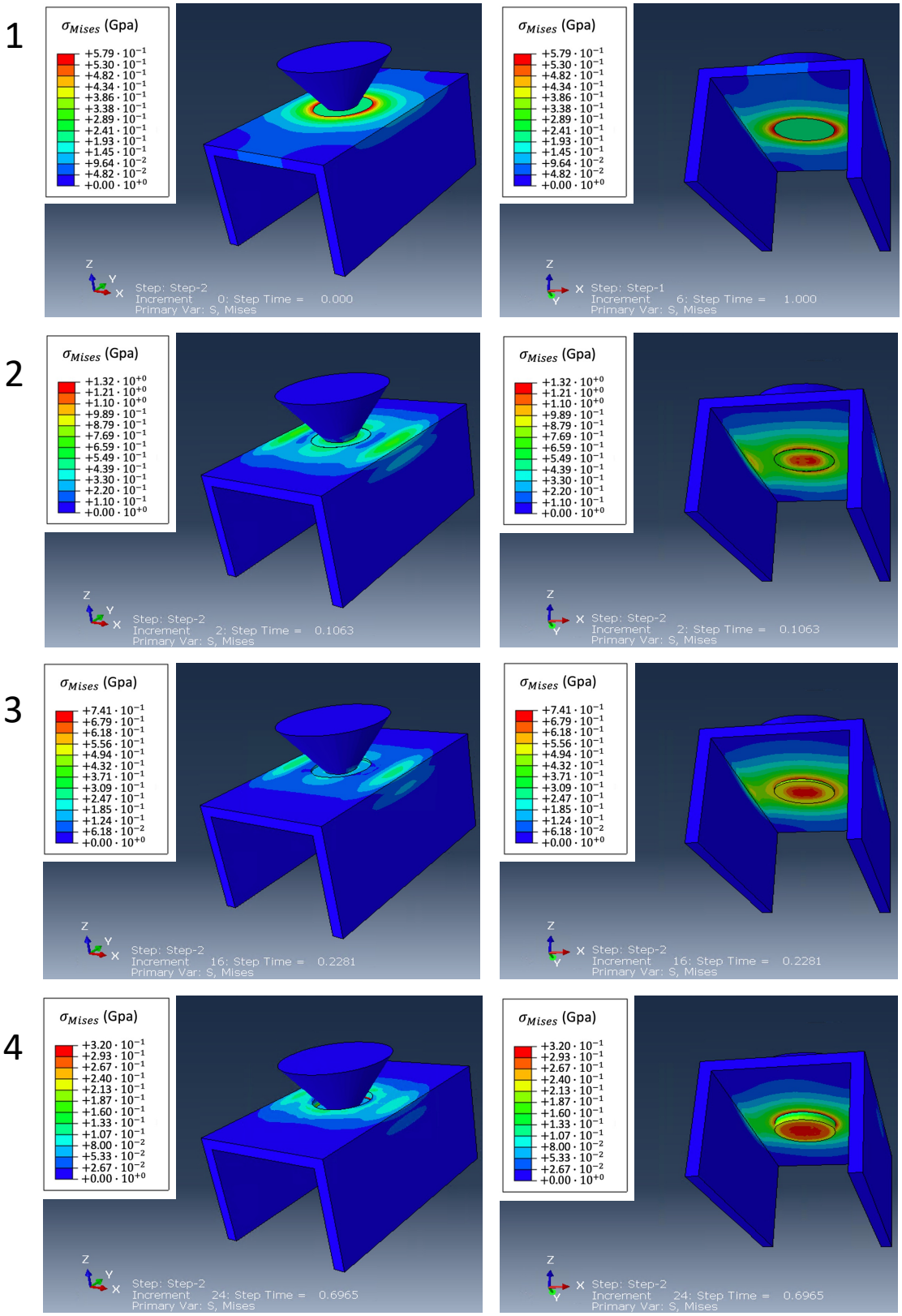

Figure I.32: Von Mises Stress profile of B4 from up and down perspectives for the different stages of indentation.